IRRADIATION RESPONSE AND MECHANICAL PROPERTIES OF 316L STAINLESS STEEL FABRICATED BY DIRECT ENERGY DEPOSITION

A Dissertation

by

CHING-HENG SHIAU

Submitted to the Office of Graduate and Professional Studies of
Texas A&M University
in partial fulfillment of the requirements for the degree of

DOCTOR OF PHILOSOPHY

Chair of Committee,	Lin Shao
Committee Members,	Sean McDeavitt
	Xiaofeng Qian
	Pavel Tsvetkov
Head of Department,	Michael Nastasi

May 2021

Major Subject: Nuclear Engineering

ABSTRACT

Additive manufacturing (AM) techniques have been widely used to fabricate structural components with complex geometries. Understanding AM materials under extreme environments is crucial for their implementation in various engineering sectors. In this study, the deformation behavior and irradiation tolerance of 316L stainless steel (SS) fabricated by the direct energy deposition (DED) process were investigated. The fabrication-induced nanopores with an average diameter of 200 nm exhibited a core-shell structure. The strain mapping around the pores suggests that the core-shell structure showed a local tensile strain. *In situ* tensile testing in a scanning electron microscope (SEM) showed a high density of deformation twins forming in the DED fabricated specimen at room temperature. Precession electron diffraction (PED) revealed that the martensitic phase transformation preferentially occurs around the nanopores. Proton irradiation experiments were performed at 360°C for both conventional and DED fabricated specimens. The DED fabricated 316L SS exhibits a stronger void-swelling resistance and lower dislocation loop density than its wrought counterpart. Fabrication-induced features, such as nanopores and sub-grain boundaries, could serve as defect sinks to absorb irradiation-induced defects. Single crystal micro-pillar compression revealed the critical resolved shear stress of AM 316L SS decreased from 106 MPa to 87 MPa after annealing and significantly increased to 246 MPa after proton irradiation. Twinning and martensitic phase transformation were developed at the later stage of deformation in non-irradiated AM 316L SS. Twinning became the primary deformation mechanism after irradiation. Irradiation hardening results were comparable with the prediction from Orowan dispersed barrier model. The model inferred dislocation loop was the primary factor to strengthen the AM 316L SS. Characterization showed radiation-induced voids could be compressed by twin or cut by dislocation while nanopores from fabrication can pin down dislocations. Although nanopores have shown the capability to strengthen the material and mitigate swelling, the residual stress and sub-grain boundary were considered the mechanical properties and swelling behavior dominator.

DEDICATION

To my parents and sister, for their unconditional support.

ACKNOWLEDGEMENTS

I would like to give special thanks to my committee chair, Dr. Lin Shao, and my mentor in Idaho National Laboratory, Dr. Cheng Sun, for their guidance and support throughout the course of this research. Their guidance and support is the reason I have been able to achieve my degree. I also want to thank Dr. Michael McMurtrey and Dr. Frank Garner for giving me academic advice for the study.

A large thank you must also be given to my friends in College Station and Idaho Falls. Aaron French, my labmate and roommate, always be my biggest support in Texas. It would make my life much more difficult without him and lose so much chance to learn about this country. Andres Morell-Pacheco, Takanori Kajihara, and Xingjian Wei, my climbing partners, have always caught me when I fell or was stressed out. And my mountaineering friends in Idaho Falls, Dave McGrath and Ross Hays, guided and encouraged me when facing challenges. Fei Teng and Xiang Liu, my colleagues and roommates in Idaho, are always supportive and willing to talk with me when I doubt myself.

I also want to thank all the technicians and staff who have assisted me in doing experiments at Texas A&M University and Idaho National Laboratory. Without them, this study would never be completed.

CONTRIBUTORS AND FUNDING SOURCES

Contributors

This work was supervised by a dissertation committee consisting of Professor Lin Shao [advisor], Professor Sean Mcdeavitt, and Professor Pavel Tsvetkov of the Department of Nuclear Engineering, and Professor Xiaofeng Qian of the Department of Materials Science and Engineering. This research involved collaboration with Dr. Cheng Sun of the Advanced Characterization Division in Idaho National Laboratory for structural characterization.

The additive manufactured 316L stainless steel was fabricated by Dr. Robert O'Brien and Randall Scott of Idaho National Laboratory. Data of STEM EDS of AM-316L was collected by Dr. Lingfeng He of Idaho National Laboratory. The proton irradiation experiment was the cooperation with Dr. Michael McMurtrey of Idaho National Laboratory and Dr. Miao Song of the University of Michigan. Dr. Jing Lu of NanoMEGAS USA assisted the visualization of strain mapping. Karen Wright of Idaho National Laboratory conducted X-ray diffraction on 316L stainless steel powder and printed product. Richard Hatch of Idaho National Laboratory fabricated the custom fixtures for *in situ* tensile tests.

All other work conducted for the dissertation was completed by the student independently.

Funding Sources

This work is supported by the Idaho National Laboratory Laboratory-Directed Research & Development Program under Department of Energy (DOE) Idaho Operations Office Contract DEAC07-051D14517. This work was also supported by the U.S. Department of Energy, Office of Nuclear Energy under DOE Idaho Operations Office Contract DE-AC07- 051D14517 as part of a Nuclear Science User Facilities experiment. L. Shao acknowledges the partial support from NNSA grant DE-NA0003921.

NOMENCLATURE

AM	Additive Manufacturing
BCC	Body-Centered Cubic
BF	Bright-Field
CRSS	Critical Resolved Shear Stress
DED	Directed Energy Deposition
DF	Dark-Field
dpa	Displacement per Atom
EDS	Energy-Dispersive X-ray Spectroscopy
EELS	Electron Energy Loss Spectroscopy
FCC	Face-Centered Cubic
FIB	Focused Ion Beam
HCP	Hexagonal Closed-Pack
HRTEM	High-Resolution Transmission Electron Microscopy
IASCC	Irradiation-Assisted Stress Corrosion Cracking
LENS	Laser Engineered Net Shaping
PED	Precession Electron Diffraction
RIS	Radiation-Induced Segregation
SEM	Scanning Electron Microscope
SNICS	Source of Negative Ions by Cesium Sputtering
SS	Stainless Steel

TEM	Transmission Electron Microscope
WBDF	Weak-Beam Dark-Field
XRD	X-ray Diffraction

TABLE OF CONTENTS

Page

LIST OF FIGURES

Page

LIST OF TABLES

CHAPTER I

INTRODUCTION

The nuclear reactor possesses an extreme environment, including high temperature, corrosion coolant, internal stress, and irradiation to materials. Although each type of reactor's operation condition is different, the reactor materials all face the challenge of degradation. Radiation-induced defects could change the microstructure and mechanical properties over time. Vacancies and interstitials created by radiation could form voids and dislocation loops, which cause material embrittlement and swelling. Figure 1 shows the radiation swelling of 316L after irradiated in a fast reactor [1]. Under stress and radiation environment, cladding materials and fuels are more prone to develop cracks. Figure 2 demonstrates the multiple degradation mechanisms through the cross-section of a fuel rod. The crack and missing piece developed in the fuel can pose a stress localized region and induce a crack in the cladding. It is critical to maintaining mechanical integrity since the degradation of materials could reduce performance and lead to safety issues. Repair and replace any part in a nuclear reactor are very difficult and expensive due to the radioactive environment and the reduction of nuclear reactor construction worldwide. Expanding the component lifetime and reducing repair or replacement costs are the main motivations to pursue better performance materials—innovative ways to fabricate materials hence to be developed.

Advanced manufacturing utilizes innovative processes to fabricate materials to improve product performance. However, materials fabricated by advanced manufacturing still need to go through detailed investigation so they can be verified to use in industry. Among those advanced manufacturing processes, additive manufacturing (AM) will be focused on this research. We will investigate the mechanical properties and irradiation response of AM-316L through microstructure evolution.

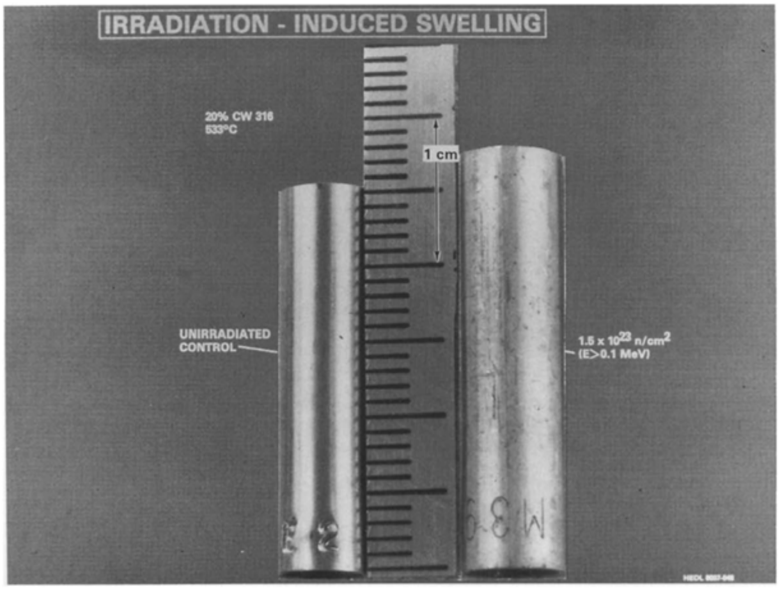

Figure 1 Radiation swelling of 316 stainless steel rod after irradiated in fast reactor at 533°C. Image reprinted from Mansur et al., 1994 [1].

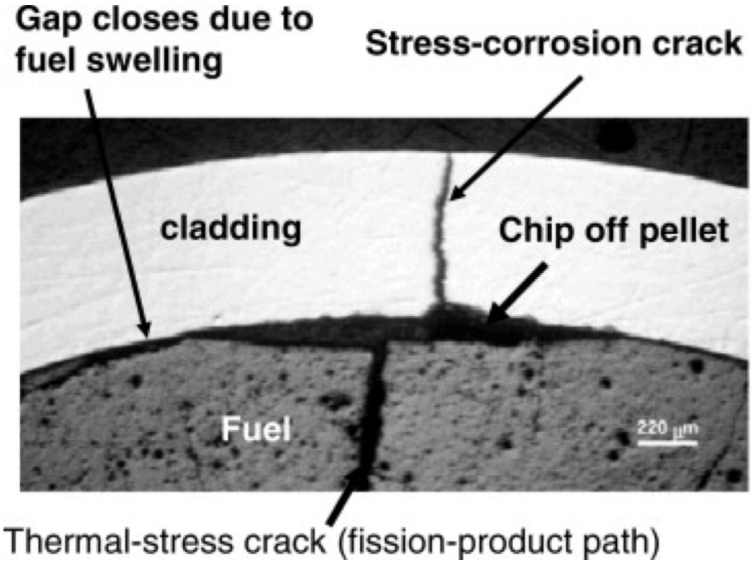

Figure 2 Degradation of nuclear fuel, showing stress corrosion cracking in cladding material, expansion and thermal stress crack in fuel. Image reprinted from Whittle et al. 2016 [2].

1.1 Additive Manufacturing

Metallic additive manufacturing (AM) is a technique using localized energy deposition to build parts layer-by-layer. Industries have started to apply AM techniques with the trend is growing in recent years. Figure 3 shows the AM market share by industry, showing industrial/business machines and aerospace have the most AM application [3]. The flexibility and rapid prototyping of AM can effectively reduce the time of early product development. American Society for Testing and Materials (ASTM) categorized AM technology into three major groups: directed energy deposition (DED), powder-bed fusion, and sheet lamination (SL) [4]. Details of classification under each category can be found in Figure 4. Powder-bed fusion, also known as selective laser melting, uses roller to distribute powder on the stage evenly. The laser or electron beam then draw out the pattern for each layer. The sample stage moves down as the layers build up. The powder-bed configuration limits the sample geometry due to the fixed stage moving direction. Sheet lamination utilizes thin metal foil to build the products instead of powder. It also has a fixed vertical building direction due to the configuration. The process used in this study, laser-engineered net shaping (LENS), falls under the DED technology. The LENS process uses a focused laser as an energy source to fuse metallic powder along the laser path. The powder is sprayed out through nozzles around the center laser beam and shielded with inert gas to the melt pool. The center nozzle has a continuous airflow to protect the laser optical components from spattering particles. Simplified schematics of the LENS system and fabrication process are plotted in Figure 5, showing the five major systems in LENS. DED techniques have a similar setup but with minor variations, such as energy source and nozzle design. Figure 6 shows the nozzle spraying out the powder with a laser beam at the center during operation. A feature of the LENS process is building functionally graded material (FGM) by customizing printing parameters [5]. FGM is a material that composition or structure gradually changes over volume. Building FGM needs to consider the compatibility of different alloys in order to create a gradient structure. An example of FGM of combining 316L SS and Inconel 625 (In625) is shown in Figure 7, where the middle layer was served as a transition region with 50% of each component.

Nonuniformity in AM materials has been reported in the literature, and strength, elongation, fracture toughness, and fatigue of AM materials could vary with different orientations [6-10]. For specific mechanical properties, like yield strength, it is possible to achieve uniformity by adjusting printing parameters [11]. Unlike conventional wrought material, the mechanical testing on AM materials had varying results in each case. The discrepancy may be due to the variation of microstructure from printing parameters [8, 12-14]. Sub-grain structure, pores, and nonuniform phases present in AM materials could also contribute to the unique mechanical behavior. The grain morphology and strong crystallographic texture observed in AM materials caused anisotropy in mechanical properties [14-16]. Kok et al. provided an overview of the anisotropy and heterogeneous properties of metal AM processes and investigated each printing parameter [17]. Ziętala et al. indicated that chemical segregation near the AM-316L SS sub-grain boundaries could result in ferrite formation [18]. The cooling rate and build temperature were reported as two significant factors determining the final phase distribution in AM products [19].

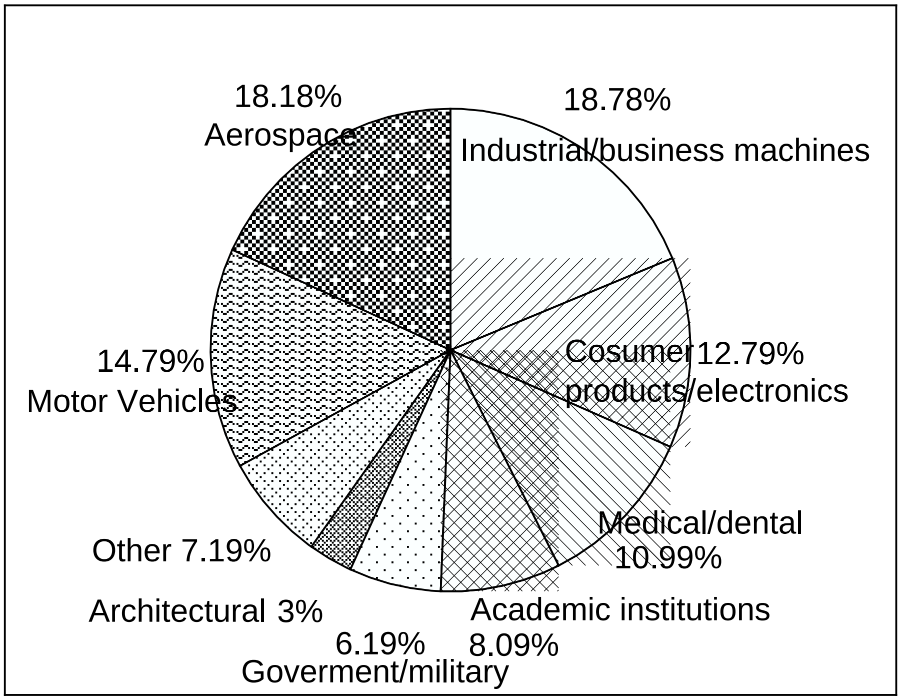

Figure 3 Additive manufacturing market share by industry in 2017. Image adapted from Joel et al., 2019 [3].

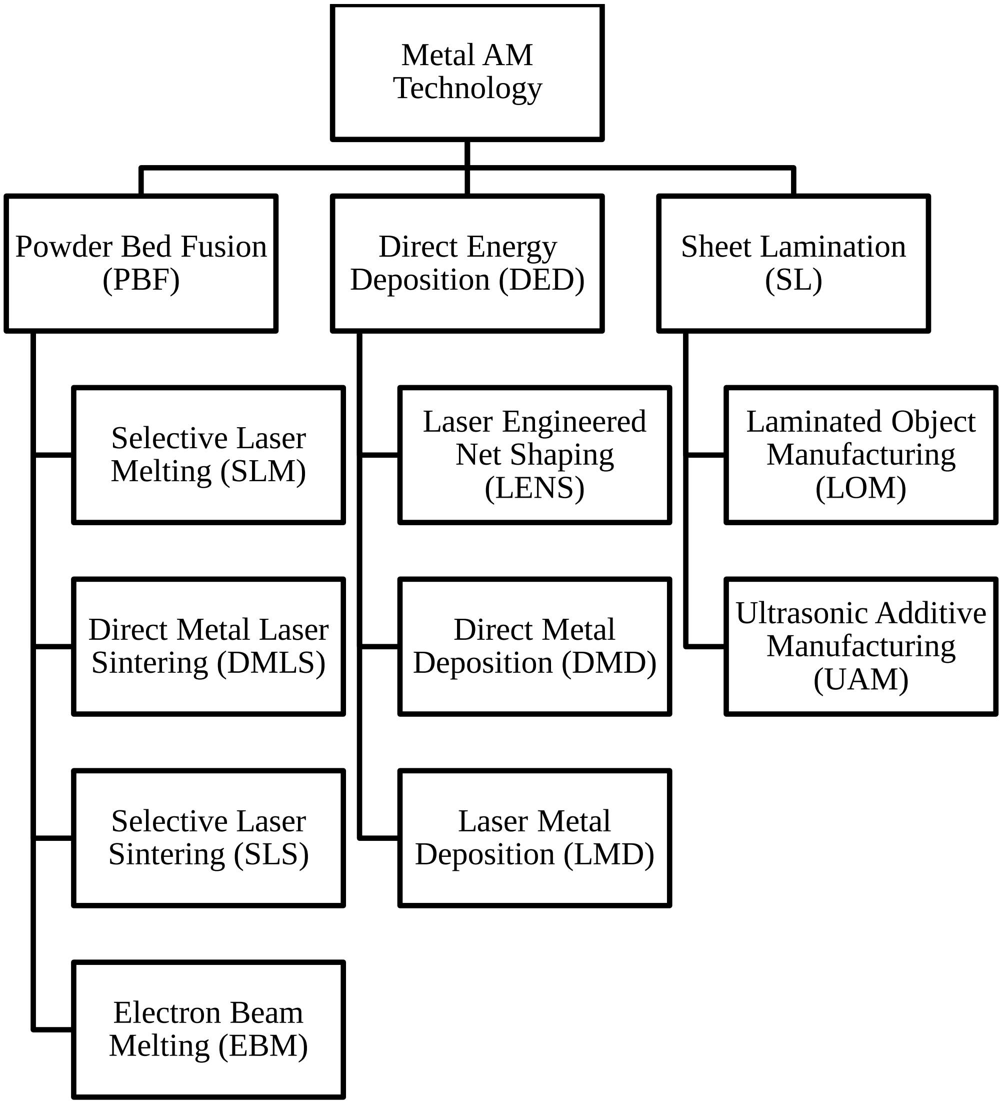

Figure 4 Showing the classification of additive manufacturing technologies.

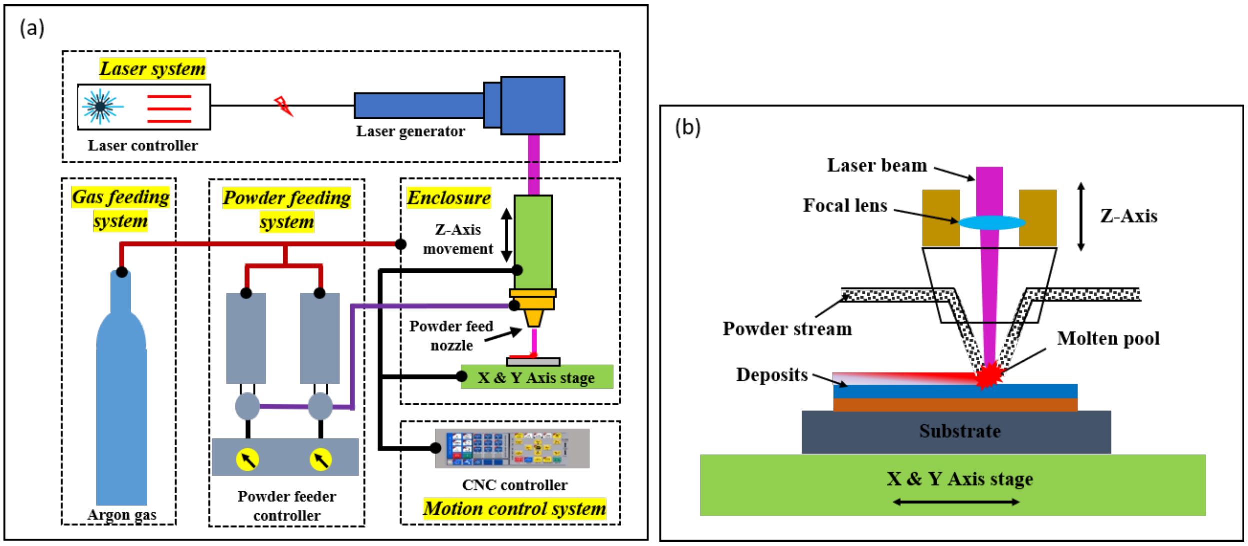

Figure 5 Schematic diagrams of the (a) LENS system and (b) nozzle.

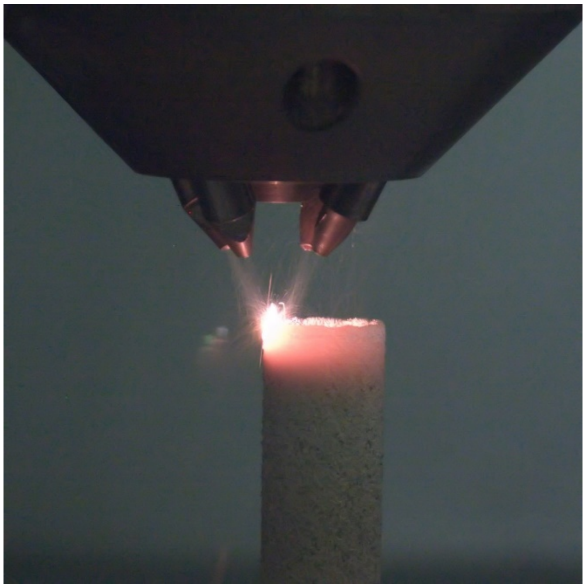

Figure 6 Showing the nozzle at operation.

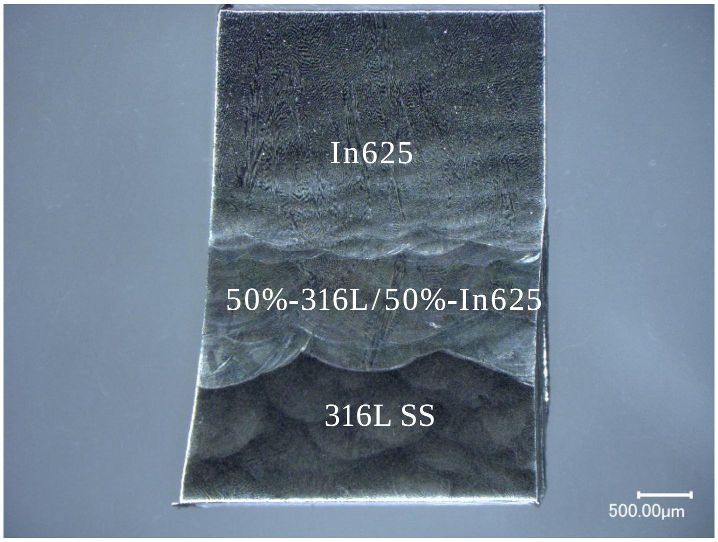

Figure 7 Showing an FGM combining 316L SS and In625.

1.2 Microstructure of Additively Manufactured Alloys

The microstructure of metallic materials fabricated by the laser-based AM technique has been extensively studied. Pore structures, induced either by powder porosity or printing process, are commonly observed in laser-based AM materials [17, 20]. In DED fabricated stainless steel, the interlayer porosity increases with the powder porosity and can be mitigated by adjusting the printing parameters [21, 22]. Thijs et al. [23, 24] reported that the formation of porosity in AlSi10Mg fabricated by selective laser melting was attributed to the incomplete melting particles and the collapse of keyholes, which are deep and narrow weld pools, during rapid solidification. The trapping of shielding gas from a high powder flow rate or the lack of fusion between the deposition layers could also lead to pores' formation [20]. Generally, spherical pores are created during the melting-solidification process, and irregular pores are due to the lack of fusion or incomplete re-melting [22, 25]. The rapid solidification and significant thermal gradient could result in phase instability in laser-based AM materials. Delta ferrite phases were present in the austenitic 316L stainless steel fabricated using DED, and the sub-grain boundaries were depleted with nickel, while enriched with chromium and molybdenum [18]. Fine ferrite phases were observed at the austenite sub-grain boundaries, and the formation of the secondary phases was related to the heat input and wire feed rate [26].

A three-dimensional model developed by Khairalla et al. was used to explain pores' evolution during the process [27]. The model illustrates the cooling process is a competition between the recoil force from heat impact and the surface tension force. The recoil effect spatters the molten material while the latter pulls the material back, and pores could be formed during the subsequent collapse. Marangoni convection driven by temperature gradient dominates after a local spot falls below the boiling point and pulls the fluid towards it or brings in incomplete melted particles. Incompletely melted particles and gaps between the laser scan could both trap pores inside the AM materials.

1.3 Mechanical Properties of Additively Manufactured Alloys

The nonuniformity of mechanical properties of laser-based AM materials has been widely reported. The strength, ductility, and fatigue of AM materials varied with locations in the printed components [6-10]. Microstructures' variation causes the discrepancy of properties during printing [8, 12-14]. The sub-grain structure, pores, secondary phases, and residual stress could lead to AM materials' nonuniform mechanical behavior. The sub-grain structure was considered as the main contributor to the hardening of AM materials [28]. The presence of pores could strengthen or weaken the materials depends on the porosity [29]. In Yang et al. study [30], AM-316L axial specimens (parallel to the printing direction) had lower yield strength and strain-to-failure than transverse specimens (perpendicular to the printing direction), and the strain-to-failure varies from 4% to 38%. A pronounced tension-compression asymmetry in yield strength and work hardening rate was reported in AM 316L SS fabricated using PBF, and they were governed by the intragranular residual stresses and associated back stresses [31].

The effects of pores on mechanical properties have been studied in previous research. Gibson and Ashby have established the relationship among yield strength, Young's modulus, and density for open-cell foams of different configurations [32]. According to their scaling relation, yield strength and Young's modulus have positive correlations with foam materials' density. The Gibson and Ashby correlation has been widely applied to study foam mechanical behaviors. Kaya et al. found the porosity and the degree of pores' openness could significantly impact the deformation mechanism [33]. Mameka et al. successfully used the Gibson and Ashby correlation to describe nanoporous gold's mechanical behavior [34]. In the study of Simone et al., the relation of tensile strength and porosity has been set up by using solid-gas eutectic solidification (GASAR) fabricated copper [29]. They found the yield strength would rise significantly at the beginning and then decrease with increasing porosity. Ultimate tensile strength would decrease linearly as the porosity increased. Li et al. developed a molecular dynamics (MD) model to describe nanopores' influence on a single crystalline CoSb3 [35]. Their results show that pores could act as a weak spot and elastic modulus, ultimate tensile strength, and yield strength would degrade with growing porosity. Both the Gibson and Ashby correlation and Li’s MD model have their limitations: the former might have a limit on the scale while the latter does not include the interaction between dislocation and pores. At the microscale level of interaction, a nanopore could act as an obstacle to retard the movement of dislocation, which results in hardening. Void dispersion strengthening is one technique to enhance AM materials’ yield strength [36]. Osetsky et al. used atomic-scale modeling to simulate the interaction between void and dislocation in face-centered cubic (FCC) structure [37]. The model illustrated that dislocation could dissociate into Shockley partials while migrating through nano void. The Shockley partials prevent dislocation climbing and could break through the void individually if the void size is smaller than 4 nm. Robach et al. studied the interaction between dislocation and void in Cu through in situ straining and ion irradiation in the transmission electron microscope (TEM) [38]. They found radiation-induced defects can pin down the propagation of dislocation, which resulted in dislocation bowing. Dislocation originated from grain boundary can form channels. Channeling can clear radiation-induced defects by multiple passages of dislocation and create a defect-free zone.

1.4 Irradiation Responses of Additively Manufactured Alloys

Radiation-induced voids and dislocation loops can interact with dislocation while deformation and strengthen the materials. Two types of strengthening mechanisms can be found in irradiated FCC alloys: source hardening and friction hardening. Source hardening is caused by radiation-induced defects close to the Frank-Read sources. The vicinity defects raised the stress required to expand and multiply the loops. Once the defects are destroyed by dislocation, a drop after yield stress can be observed. Figure 8 shows the drop in the yield stress and the change of stress-strain curves of irradiated FCC alloys. The increase of yield stress accompanies the decrease of elongation as the dose increase.

Friction hardening refers to the stress required for dislocation propagation. Dislocation stress fields can interact with each other and cause long-range stresses. Obstacles such as defect clusters, loops, precipitates, and voids create short-range stresses while interacting with a moving dislocation. Figure 9 demonstrates possible interaction mechanisms between dislocation and obstacles. Dislocation will bow and form a loop around an impenetrable obstacle. Weak obstacles might be cut through by dislocation and form a step with the width of a Burgers vector. Bowing is also possible when dislocation interacts with voids or precipitates. Orowan dispersed hardening model can be used to estimate short-range hardening. The sum of long-rang and short-range stresses is the shear stress required to move the dislocation.

The fundamental study of AM materials under extreme conditions is critical for the nuclear application of AM components. A few studies reported the response of AM materials to irradiation environments. Shang et al. [39] observed that the cellular dislocation walls in the sub-grain boundaries could serve as effective defect sinks by absorbing dislocation loops under in situ Kr ion irradiation. They also observed that irradiation might change the sub-grain structures. Song et al. [40] reported the anisotropy in both tensile properties and irradiation-assisted stress corrosion cracking (IASCC) susceptibility in PBF fabricated 316L stainless steel and recommended post-printing hot-isotropic pressing to enhance irradiation tolerance and IASCC performance.

Phase stability is another concern in irradiation responses [41]. Radiation-induced segregation (RIS) can have a significant effect on phase formation or dissolution. Defect sinks, such as free surface, grain boundary, and dislocation, attract vacancies and interstitials during irradiation. The fluxes of defects are associated with atom fluxes. Any preferential or difference association of defect fluxes with a certain component will create a buildup or depletion close to the defect sink. The local chemical changes in structural materials could increase the susceptibility to intergranular corrosion and stress corrosion cracking. RIS has been observed in austenitic, ferritic, and zirconium alloys. In 316L alloys, Cr depletion and Ni enrichment were observed at the grain boundary. The lack of Cr at grain boundary to form a thin passive layer of Cr2O3 can lead to intergranular corrosion, which is a threat to the integrity of structural components. Temperature is a critical factor for RIS. At low temperatures, defects generated by radiation have low mobility. The high corresponding defect concentration leads to a higher defect recombination rate, which reduces RIS. At high temperatures, the high number of thermal-induced defects and high defect mobility promotes defect recombination rate. RIS is also suppressed at high temperatures. RIS can notably occur at intermediate temperature. The relatively low concentration of thermal-induced and radiation-induced defects leads to low defect recombination rates, leading to significant RIS. Figure 10 shows the temperature dependence curve of RIS in a nickel alloy after proton irradiation, showing RIS was maximized at the temperature between 350°C and 400°C [41].

Other mechanisms that govern RIS include composition gradient, solute size, radiation dose rate, and impurities. RIS can significantly change the composition close to the sink. Therefore, the diffusion driven by the composition will be modified. The diffusion from the composition gradient is in the reverse direction from RIS and has to be considered to estimate the composition profile accurately. As for the effects of solute size, the oversize solutes tend to interact with vacancies to release strain, leading to the depletion at defect sinks. The undersize solutes will preferentially stay or exchange site with interstitial positions, which results in enrichment at defect sinks. In austenite alloys, Cr is an oversize solute, and Ni is an undersize solute. The radiation dose rate can shift the RIS temperature dependence. The low dose rate shifts the RIS toward a lower temperature. At low temperatures, the lower defect generation rate with the same mobility reduces the defect recombination rate and enhances the sink's effects, resulting in more significant RIS. At high temperatures, a lower displacement rate has little effect on defect recombination rate but lowers the overall defects generation rate. The lower defect concentration leads to less segregation at high temperatures. Impurities in the materials could interact with defects and modify the flux, and this interaction will modify RIS as well.

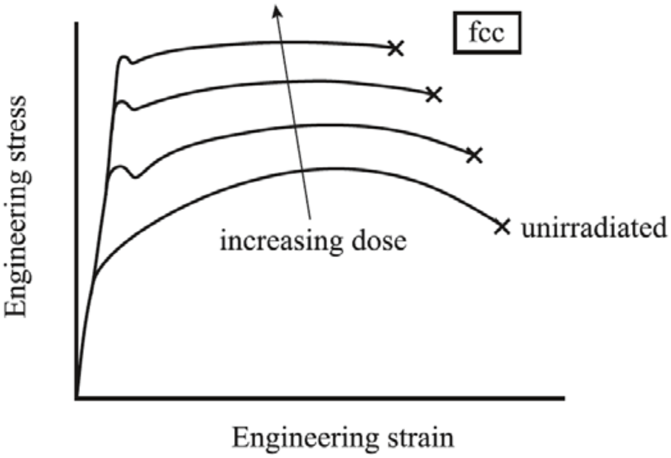

Figure 8 Irradiation hardening evolution with the increase of dose in FCC alloys. Image reprinted from Was et al., 2007 [4].

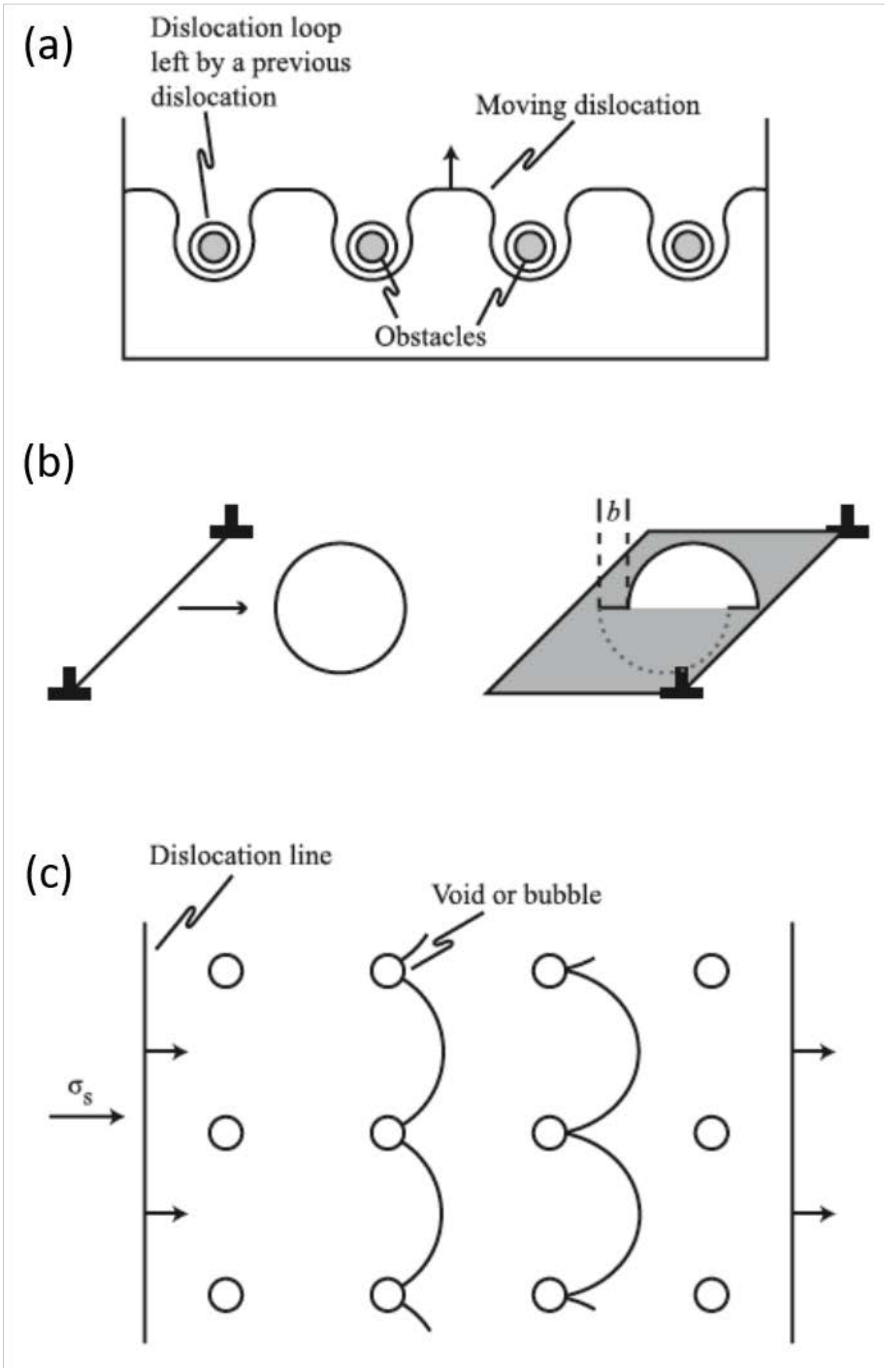

Figure 9 Schematic diagrams of dislocation (a) bowing around impenetrable obstacles, (b) cutting through an obstacle and (c) pinned down by voids or bubbles. Image reprinted from Was et al., 2007 [4].

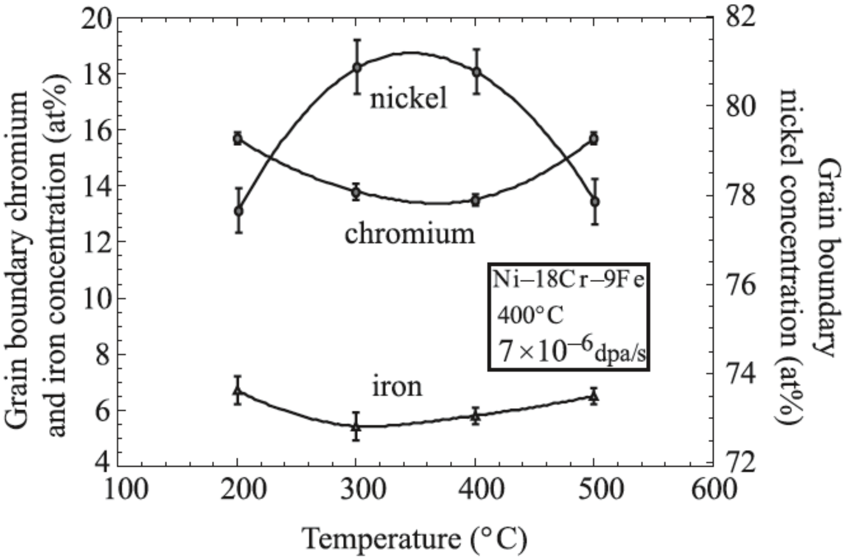

Figure 10 Temperature dependence of RIS at grain boundary Ni, Cr, and Fe in a Ni-18Cr-9Fe alloy irradiated with 3.4 MeV proton at 400°C to 1 dpa with the displacement rate at 7×10^{-6} dpa/s. Image reprinted from Was et al., 2007 [4].

1.5 Motivation and Objectives

316L SS has been used as structural materials in light water reactors. Moreover, 316L SS is a candidate to be used in generation IV reactors. The lack of knowledge on how advanced manufacturing process affects microstructure brings us the uncertainty on properties. Especially for additive manufacturing, printing parameters are critical to microstructure, yet it is still unclear how printing parameters relate to the final product. Most of the studies took pores as undesired features and try to eliminate them in the additively manufactured alloy. However, in our view, those pores are unique in additively manufactured materials and have the potential to improve irradiation tolerance.

In this study, 316L stainless steels were fabricated using the DED technique in a LENS system. The printed microstructure and its evolution under tension tests were characterized and correlated to the mechanical properties using *in situ* scanning electron microscopy. Proton irradiation experiments were performed for both AM and wrought 316L stainless steel at identical conditions. The changes in mechanical properties after proton irradiation were investigated by micro-pillar compression tests. Figure 11 shows the experiment flow chart of this project. This study provides new insights into understanding the influence of AM features on deformation behaviors and irradiation tolerance.

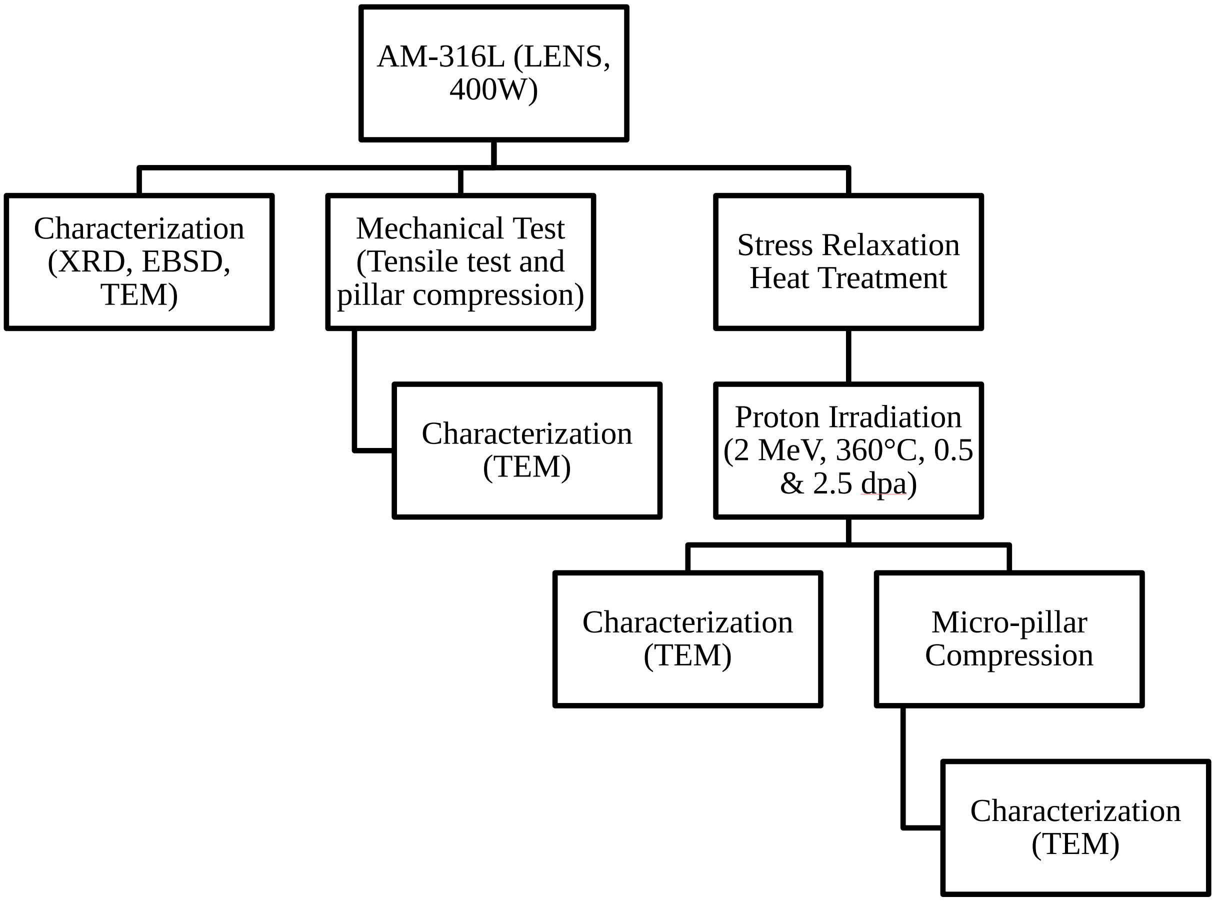

Figure 11 Experiment flow chart to characterize AM-316L SS.

CHAPTER II

EQUIPMENTS AND EXPERIMENTAL TECHNIQUES

2.1 X-ray Diffraction (XRD)

XRD technique utilizes Bragg's diffraction law, see equation (2.1), to investigate the microstructure of materials.

$$n\lambda = 2dsin\theta \tag{2.1}$$

Where n is a positive integer, λ is X-ray wavelength, d is the interplanar distance, and θ is the incidence angle. Figure 12 shows the X-ray scattering diagram to illustrate the relationship of each parameter. The coherent elastic scattering X-ray can provide the material information, including phases, grain size, and strain. This study used XRD to investigate the phases in 316L SS powder and as-manufactured product, using Cu Kα radiation. XRD data were analyzed by GSAS-II, a Python-based general-purpose package for diffraction data analysis developed by Argonne National Laboratory. GSAS-II analyzed the data with Rietveld refinement to obtain lattice parameters and phase fraction [5]. Rietveld refinement is briefly described as follows, and details can be found in the reference [6-9]. The powder diffraction intensity I_obs at the scattering angle $2\theta_i$ of Rietveld is calculated according to the following equation:

$$I_{cal} = S\sum\nolimits_{K} L_k |F_K|^2 \varphi(2\theta_i - 2\theta_K) P_K A + B_i \tag{2.2}$$

where K represents index (hkl) of Bragg reflections contributing to the intensity at the point i. S is phase scale factor. L_k contains Lorentz, polarization. And multiplication factors. F_K is structure factor for Bragg reflection. φ is profile function determined by diffractometer. P_K is orientation factor. A is the absorption factor. y_{bi} is background at the point i. In the refinement, the calculated pattern is refined by minimizing the weighted residual factor R_{wp}:

$$R_{wp} = \frac{\sqrt{\sum_i w_i |I_{obs}(\theta_i) - I_{cal}(\theta_i)|^2}}{\sqrt{\sum_i w_i |I_{obs}(\theta_i)|^2}} \tag{2.3}$$

where $w_i = 1/I_{obs}(\theta_i)$. Lattice parameter and phase fraction can be obtained after peak intensity and location are matched. R_{wp} below 10% is usually considered a good fit. The details of determination of R_{wp} can be found in the reference from Toby [10].

Full-width half-maximum (FWHM) needs to be refined as well. The peak shape observed in the synchrotron spectrum is the combined results of sample properties and instrument. Sample properties, including grain size, stress/strain, and defects, could contribute to peak broadening. Figure 13 demonstrates the effects of instrumental, grain size, and strain broadening on the FWHM, assuming the material is a perfect single crystal. Deconvolution of the peaks from the instrumental broadening need to be done first before calculating grain size and dislocation density. The peak approximation function in GSAS-II is the pseudo-Voigt function. Pseudo-Voigt is a linear function of Gaussian and Lorentzian components. GSAS-II uses the parameters U, V, W in Gaussian function and X, Y in Lorentzian function to fit the observed FWHM Γ:

$$\begin{aligned} \Gamma = (&\Gamma_G^5 + 2.69269\Gamma_G^4\Gamma_L + 2.42843\Gamma_G^3\Gamma_L^2 + 4.47163\Gamma_G^2\Gamma_L^3 \\ &+0.07842\Gamma_G\Gamma_L^4 + \Gamma_L^5 \end{aligned} \tag{2.4}$$

$$\Gamma_G = (U\tan^2\theta + V\tan\theta + W)^{\frac{1}{2}} \tag{2.5}$$

$$\Gamma_L = \frac{X}{\cos\theta} + Y tan\theta \tag{2.6}$$

where Γ_G and Γ_L are the FWHM of Gaussian and Lorentzian, respectively. Optimization of peak shape is done by minimizing R_{wp} as described above.

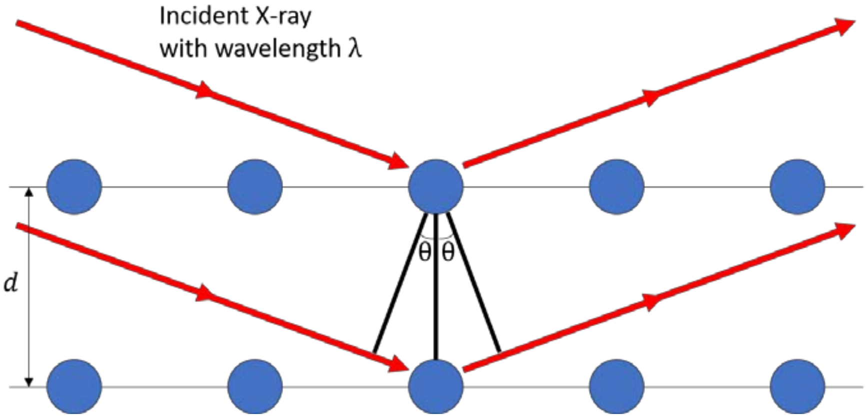

Figure 12 A schematic diagram of X-ray scattered from lattice atoms.

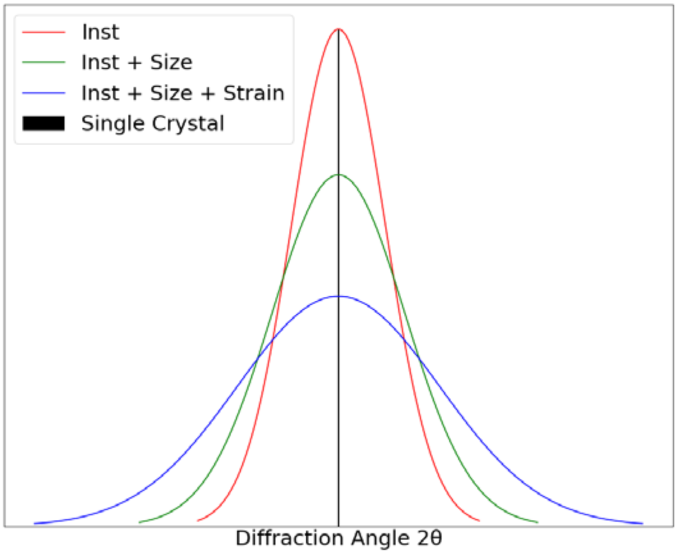

Figure 13 XRD peak profiles, showing the effects of instrumental, grain size, and strain broadening on FWHM.

2.2 Electron Backscatter Diffraction (EBSD)

EBSD is a technique based on Bragg's reflection from inelastically scattered electrons in a scanning electron microscope (SEM). Backscattering electron is highly sensitive to the surface condition. The detection depth of 20 kV electron is about 100 nm [11]. The sample surface must be mechanically polished to flatten the surface and then electropolished to remove the deformation layer. Electropolishing solution and parameters depend on the material. Perchloric acid is the universal solution to polish most alloy systems. However, due to the strong oxidizing power and the risk of forming shock-sensitive explosive perchlorate salt, perchloric acid must be handled in the fume hood with a wash-down function and cooled with liquid nitrogen during electropolishing. Other kinds of acids could be used as replacements if perchloric acid handling is not under safety regulations. In this study, perchloric acid and a substituted acid, a mixture of sulfuric and phosphoric acid, were utilized to polish samples and achieved equal surface condition quality.

The frontmost of EBSD detector is a phosphor screen. Inelastically scattered electrons distribute large angles and form a pair of excess and defect lines, which constitute Kikuchi pattern. The phosphor screen captures the Kikuchi pattern and saves it with the corresponding pixel location in a SEM micrograph. By indexing the Kikuchi pattern, the phase and orientation of the materials can be obtained. EBSD can identify smaller features than regular broad beam XRD due to its fine electron beam spot size. However, EBSD also possesses more dimension limitations and less detection depth than XRD. The sample dimension has to fit into a SEM and must not interfere with the data collection of EBSD detector. EBSD data can be used for grain orientation and size determination, phase identification, and strain analysis. It is also possible to combine EBSD and energy-dispersive X-ray spectroscopy (EDS) to collect data simultaneously. This technique is beneficial in analyzing the sample with composition gradient or multiple phases.

2.3 Mechanical Testing

In situ tensile test in this study utilized MTI tensile testing device, as shown in Figure 14. The device was loaded into a SEM to perform a tensile test with SEM recording the process. The load cell in the device was from Honeywell with 4,450 N rated. Due to the reading of force in load cell is based on the change of electric resistance, the working temperature of load cell need to stay constant during the test. The deviation can be removed by powering on the load cell at least 20 mins before the test. The position sensor of the device was a laser encoder, which spatial resolution can reach several micrometers. Custom sample holders were fabricated from 17-4 stainless steel to avoid sample sliding. The holders were precipitation hardened with heat treatment at 482 ± 8.4 °C for 60 mins with air cooling to prevent deformation during testing. The two ends of the tested sample must be covered or pressed down on the holder to prevent bouncing at breaking and damage the microscope polepiece.

Micro-pillar compression tests were conducted with Hysitron TI-950 Triboindenter with 20 µm flat-punch tip and high-load transducer. Optic-probe tip calibration was performed right before the compression test to locate the pillar precisely. The compression test used a constant strain rate to avoid the variation of the deformation mechanism. The compressed pillar was imaged by SEM then fabricated into TEM lamella to investigate the deformation mechanism.

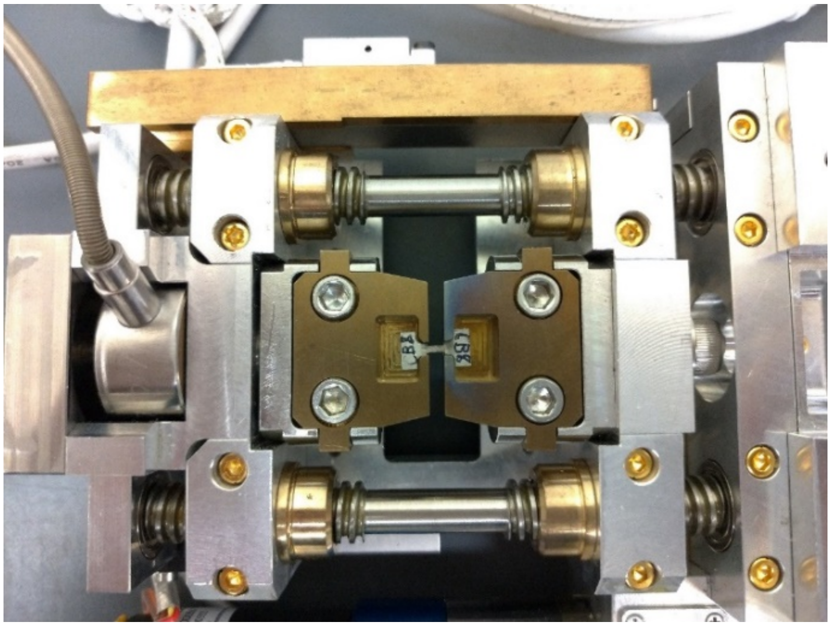

Figure 14 Photograph of the *in situ* tensile device.

2.4 3 MV Pelletron Accelerator

The 3 MV pelletron accelerator used for proton irradiation was made by National Electrostatics Corporation. The accelerator comprises three major sections: injection beamlines, pelletron, and high energy beam lines. Source is the first part on injector, followed by a bending magnet and focusing system. Source of negative ions by cesium sputtering (SNICS) was used to generate proton ions. In SNICS source, a positive voltage was applied to the target cathode. Cesium negative charged ions created by the ionizer will bombard the target cathode and sputter out the negative charge target ions. The negatively charged target ions are extracted by extractor with positive voltage and pre-accelerated to enter the injection beamline's focusing system. The focusing system maintains the ion beam at the center of the beamline and not dissipating.

The center of pelletron section is the high voltage terminal located within the pressure vessel. The terminal is charged by the pelletron chains, which are made of metal pellets. The metal pellets transport positive charges to the terminal and carry out negative charges. Figure 15 shows the internal structure of the pressure vessel. The terminal is the stainless steel column located at the center, surrounded by acceleration tubes. It is necessary to reverse the charge of the ion at the terminal to keep accelerating the particles. The gas tripper on the beamline underneath the terminal releases a small amount of stripper gas, usually nitrogen, to reverse the charge of ions to positive, as shown in Figure 16.

High energy beamlines consist of a focusing system, switching magnet, and target chamber. The switching magnet on high energy end requires a much higher current than the magnet on low energy beamlines due to the high energy of the ion beam. Depending on the experiment’s requirements, a defocus beam or raster-scanned beam can be delivered to the target chamber. Beam current and uniformity can be monitored by the Faraday cup and beam profile monitor. The beam profile monitor uses a rotating helical wire to track the beam cross-section by secondary electrons without significantly interrupting the beam. Irradiation temperature is measured by the thermocouple attached to the stage.

Figure 15 Inside the 3 MV accelerator pressure vessel, showing the terminal column at the center and the surrounding acceleration tubes.

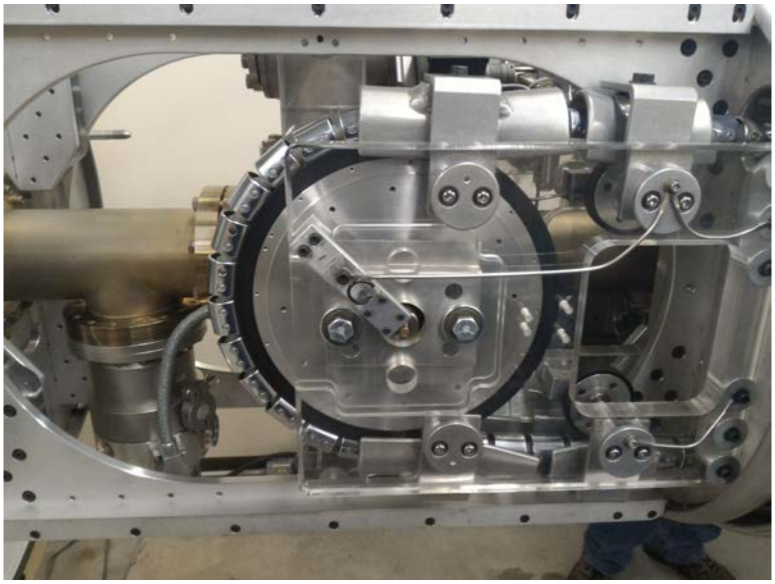

Figure 16 Internal of the terminal, showing the pellet chain at the front and gas stripper on the beamline.

2.5 Transmission Electron Microscopy (TEM) Analysis

The evolution of microstructure is a crucial factor for materials' mechanical properties. TEM analysis is probably the most widely used method to investigate the atomic scale's radiation-induced defects and deformation mechanism. This section briefly introduces the TEM analysis process and the technique used in this research.

2.5.1 TEM Specimen Preparation

TEM lamellae were prepared by the FIB technique. FIB technique is preferred over twin-jet polishing due to post-irradiation characterization is location-sensitive and with limited ion-range. It is crucial to maintain the surface integrity to obtain the location information of the area of interest. A layer of platinum was deposited on the sample to protect the surface before ion milling. Ion trenching was done on both sides of the deposited platinum layer. Then the lamella was lifted and attached to the copper grid for thinning. Both sides of the lamella were polished down to the same condition with the identical voltage to the electron transparent thickness, 50 to 100 nm. Figure 17 shows the TEM lamella before lifted out from bulk sample and after the final thinning. Final thinning was done by 2 kV ion to reduce the damage from thinning process.

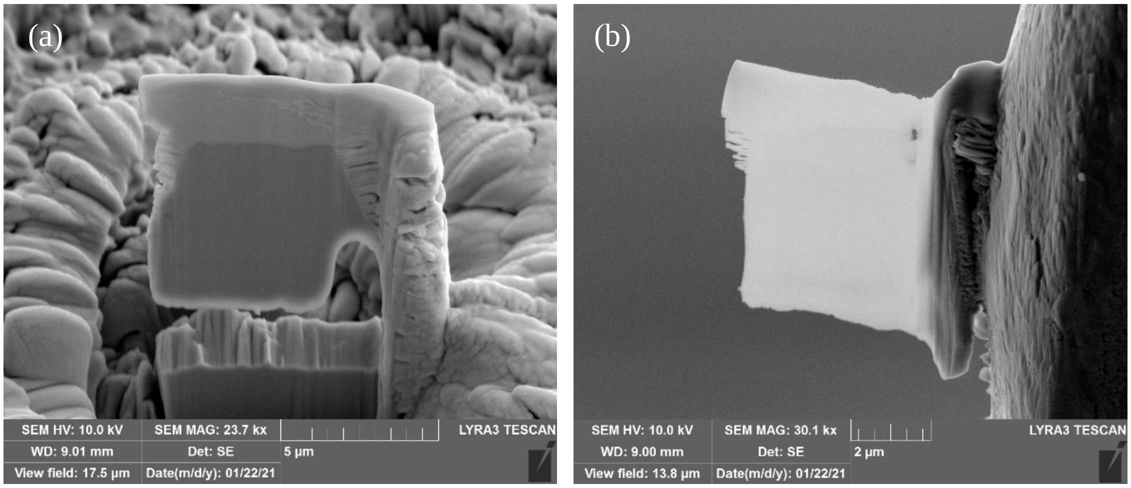

Figure 17 SEM micrographs of the process of TEM lamella fabrication, showing (a) the lamella before lifted from bulk sample and (b) the lamella after polishing.

2.5.2 TEM Basic Principle and Imaging Conditions

TEM acquires information from the interaction between materials and accelerated electrons, usually operated at 200 kV and 300 kV. TEM can provide much higher resolution than optical microscope due to electron has a shorter de Broglie wavelength than photon. Higher operation voltage of TEM can provide larger penetration depth and higher resolution, but with the risk of introducing radiation damage to the specimen. The consist of TEM micrographs is based on the electron scattering. Elastic scattering electrons provide the contrast of micrographs and gives the information of crystal structure through diffraction pattern. Inelastic scattering electrons can be used for composition analysis and thickness calculation through electron energy loss spectroscopy (EELS). Details of EELS can be found in the next section.

TEM contrast changes with focusing condition, which leads to the void size variation at different focusing depth. Figure 18 shows the change of contrast on voids at under-focus 1.5 µm, in-focus, and over-focus 1.5 µm. The thickness of the specimens was measured with EELS. Swelling rate (S) was calculated by the equation:

$$S = {}^{V_v}/_{V_t - V_v} \tag{2.7}$$

where V_t is the total volume of sample and V_v is the volume of voids. The error of swelling rate σ_s is calculated from the multiple measurements of specimen thickness t in the analysis region by standard deviation σ_t and error propagation with the equations:

$$\sigma_t = \sqrt{\frac{\sum_i^n (t_i - \bar{t})^2}{n - 1}} \tag{2.8}$$

$$\sigma_s = \frac{S\sigma_t}{\bar{t}} \tag{2.9}$$

where t_i is the thickness of ith measurement, $\bar{t}$ is the sample's mean, and n is the number of sampling.

Frank dislocation loops was characterized by relrod method [12]. Relrod technique is a weak-beam dark-field method (WBDF). The idea of using WBDF to image dislocation loops is enhancing the loop contrast by tilting the specimen away from Bragg's condition, which means a high deviation parameter [13]. The strain close to the loops may bend the reflected plane to satisfy Bragg's condition. This leads to relatively high intensity of dislocation loops in the surrounding black background.

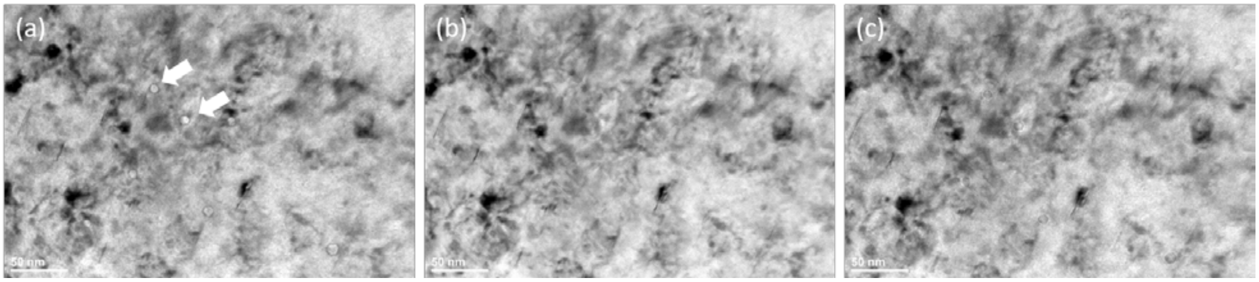

Figure 18 TEM micrographs of the voids changes with focusing condition in proton-irradiated AM-316L SS. (a) under-focus 1.5 µm, (b) in-focus, and (c) over-focus 1.5 µm. Arrows in (a) indicate the voids.

2.5.3 Electron Energy Loss Spectroscopy (EELS)

EELS is a technique based on the energy loss when an electron is scattered from an atom. Each element has its distinct energy loss spectrum, which makes composition analysis possible. Figure 19 shows a simplified diagram to demonstrate the source of signals for EELS. EELS detector located at the bottom of the sample and receive transmitted and inelastic scattered electron beam. There are three major regions in the EELS spectrum: zero loss region, low loss region, high-loss region. Each region contains specific information for characterization. Zero loss is the most intense peak. The zero-loss signal can provide higher resolution and contrast images and diffraction patterns free of chromatic aberration and diffuse-scattering effects by coordinating with the energy filter. The low-loss region reflects the interaction between the accelerated electrons and loosely bound conduction and valence-band electrons. The High-loss region covers ionization edges, which are used for composition analysis, especially for light elements. The thickness t of the sample can be calculated from the intensity ratio of zero-loss peak and the whole spectrum by the equation:

$$t = \lambda \ln \left({}^{I_t}/_{I_0} \right) \tag{2.10}$$

where λ is the mean-free path of the electron, which depends on the accelerated voltage and material composition. I_t is the total intensity of the spectrum, including zero-loss peak and all inelastic scattering region. I_0 is the intensity of the zero-loss peak. Figure 20 is an example of the EELS spectrum of 316L SS, with the arrows showing zero-loss peak and inelastic scattered region. This study used pure iron to estimate electron mean-free path, 81 nm under 300 kV, as it is the major element in 316L SS. Mean-free path estimator is a DigitalMicrograph plugin written by Mitchell based on the studies from Malis et al. and Iakouboskii et al. [14-16].

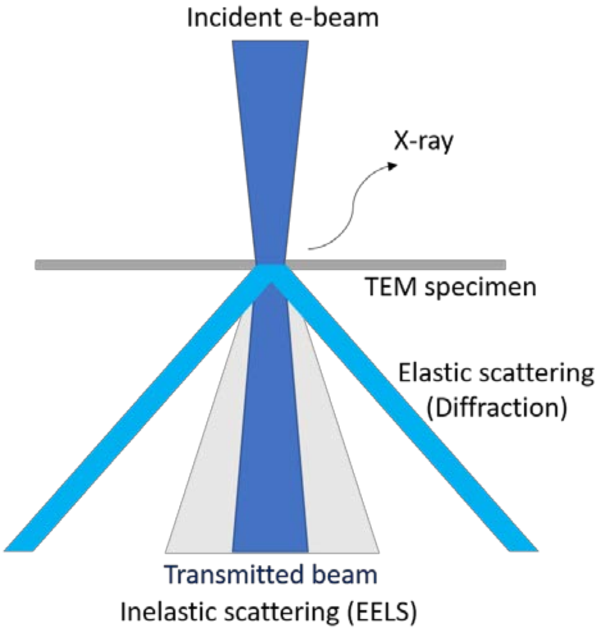

Figure 19 Diagram of the signals for EELS.

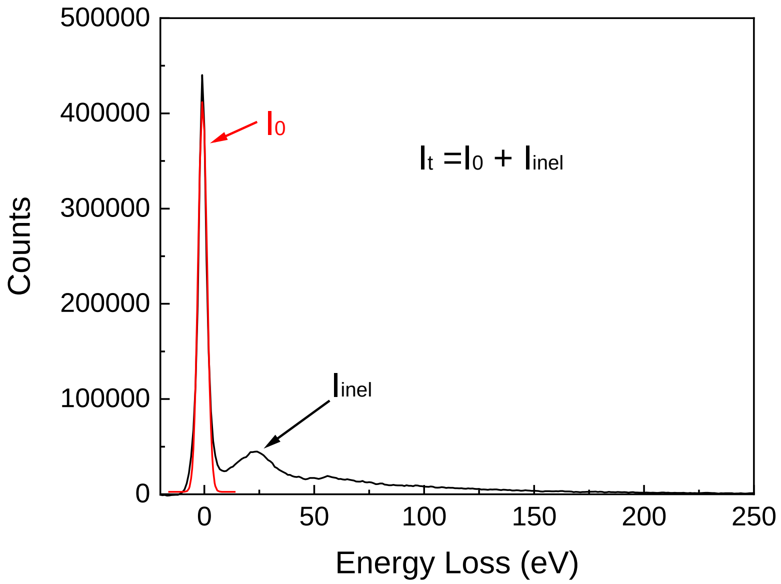

Figure 20 Example of an EELS spectrum of 316L SS, showing the zero-loss peak in red curve and elastic region in black curve.

2.5.4 Strain and Orientation Mapping with Precession Electron Diffraction

Nanobeam diffraction is a technique using a converged electron beam to investigate the material structure in nanometer size. Cooper et al. have utilized nanobeam diffraction spectrum images to obtain the material's strain distribution [17]. However, nanobeam diffraction is highly sensitive to thickness change and possesses strong dynamical effects. These challenges can be mitigated by combining nanobeam diffraction with beam precession. High-frequency precession can include higher-order diffractions intercepted by the Ewald sphere and average out dynamical effects. Figure 21 demonstrates the beam precession with the comparison of with and without precession. The diffraction pattern became more explicit and more uniform. Higher-order diffraction spots were included with the beam precession. Higher-order diffractions are more sensitive to strain than lower-order diffractions. The strain analysis can be carried out more precisely. The strain was calculated by the lattice distortion extracted from the PED patterns by a geometric phase analysis algorithm [17, 18]. Geometric phase analysis algorithm is a digital signal processing method that uses fast Fourier transform to identify any displacement in the diffraction pattern. Virtual bright-field micrographs can be brought out from the spectrum image to show the diffraction contrast.

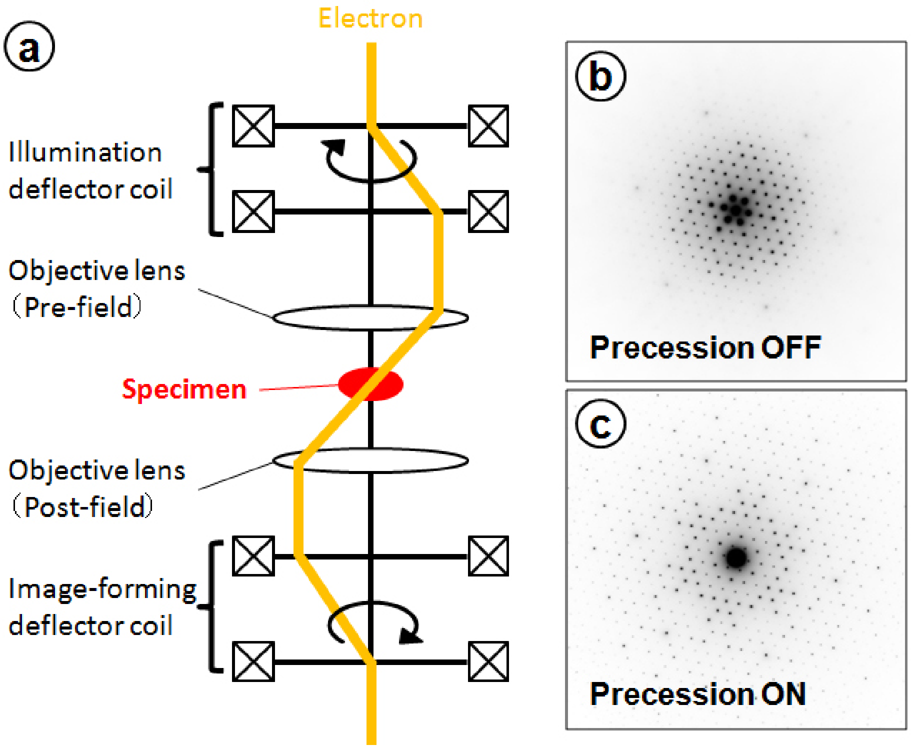

Figure 21 (a) Diagram of TEM beam precession configuration. (b) Diffraction pattern without beam precession. (c) Diffraction pattern with beam precession. Image reprinted from Tanaka [19].

CHAPTER III

MICROSTRUCTURE CHARACTERIZATION AND IRRADIATION RESPONSES*

3.1 Experimental Procedure

3.1.1 Direct Energy Deposition

AM 316L SSs were fabricated with a DED process in a LENS MTS 500 printer from Optomec Inc. The 316L SS powders were purchased from John Galt Steel. Cubes with dimensions of 10 × 10 × 10 mm^3 were printed on a 316L SS substrate with laser power of 400W, beam spot size of 600 μm, at a scanning speed of 12.7 mm/s in an argon atmosphere. A crosshatch pattern with a spacing of ~250 μm between scanning paths was employed during printing. No active cooling was utilized during printing. The wrought 316L SS purchased from Goodfellow was taken as a reference specimen in this study. The chemical compositions of the wrought and AM specimens, as listed in Table 1, were analyzed using inductively coupled plasma (ICP) and Laboratory Equipment Corporation (LECO) combustion methods.

3.1.2 Mechanical Testing

Uniaxial tensile tests were performed on wrought and AM-316L SS at room temperature in a FEI Quanta 650 FEG SEM. To directly observe the microstructure

---

*Part of the data in this section is reprinted of the open access journal from “Deformation behavior and irradiation tolerance of 316 L stainless steel fabricated by direct energy deposition” by C.-H. Shiau, M.D. McMurtrey, R.C. O’Brien, N.D. Jerred, R.D. Scott, J. Lu, X. Zhang, Y. Wang, L. Shao, C. Sun, Materials & Design, Volume 204, June 2021.

evolution under a tension test in SEM, dog-bone specimens, with a reduced gauge length of 2 mm, were prepared by electrical discharge machining. The dimension of the tensile specimens is shown in Figure 22. Tensile tests were performed for the printed specimens vertical and parallel to the substrate. AM-316Lv and AM-316Lp denote the specimens vertical and parallel to the substrate, respectively. A constant strain rate of 1×10^{-3}/s was applied during the test.

Traditional tensile tests were also conducted on annealed AM-316L treated at different temperatures to see the effects of residual stress. Figure 23 shows the change of stress-strain curve after annealing and the specimen dimension, with the sample dimension at the side. The evolution of sub-grain structures is displayed in Figure 24. This part of the work was published as a separate study in [20]. The study has found annealing at 983°C for 45 mins followed by water quenching can effectively remove internal strain without totally removing sub-grain boundaries. Therefore, 983°C annealed AM-316L SS was selected for further irradiation and characterization study.

3.1.3 Proton Irradiation

Proton irradiation experiments were performed for both wrought and AM-316L SS in a Pelletron tandem accelerator in the Michigan Ion Beam Laboratory at the University of Michigan. Specimens were irradiated with 2 MeV proton raster-scanning beam at 360°C to a fluence of 1.09×10^{19} cm^{-2} and 5.42×10^{19} cm^{-2}. The irradiation temperature determination was based on the previous studies to simulate neutron damage in a boiling water reactor (BWR) [21]. The Stopping and Range of Ions in Matter (SRIM) program with a Kinchin-Pease method was used to estimate the displacement damage in

316L SS. The displacement energy of each element used in the calculation was chosen from ASTM E521 [22]. As seen in Figure 25, the displacement damage is around 0.35 and 1.80 displacement per atom (dpa) at a depth of 5 µm. As-manufactured AM-316L SS (AM-316L) underwent a stress relaxation heat treatment at 983°C for 45 mins. A previous study indicated that annealing at 983°C for 45 minutes can effectively remove strain while still retaining sub-grain boundaries [20]. The specimens' surface for irradiation was flash-electropolished using 10% perchloric acid in a methanol solution at a voltage of ~ 30V and temperature of -40°C.

3.1.4 Microstructure Characterization

The microstructures of the wrought and AM-316L SS were characterized using X-ray diffraction (XRD) and scanning electron microscopy (SEM) equipped with an electron backscatter diffraction (EBSD) detector. The XRD experiment was conducted by Malvern Panalytical Empyrean diffractometer. The specimens were mechanically polished, followed by electropolishing in a solution of 15.4% water, 46.1% H_3PO_4, and 38.5% H_2SO_4 with a 4V potential for 13 seconds. XRD experiments were performed using Cu Kα radiation, scanning from 20° to 120° with the step size of 0.0263°. An FEI Quanta FEG 650 SEM was used to characterize the grain morphology and phase components. Strain mapping of the pore structures in the AM 316L SS and phase mapping of the deformed specimens were performed using PED with Topspin software from NanoMEGAS in an FEI Tecnai TF30 transmission electron microscope (TEM). A precession angle of 0.6^o was used for the strain mapping of the pore structures in the as-manufactured specimens and 0.48^o for the phase mapping of the tensile tested specimens.

The strain and orientation mappings were performed by collecting a series of precession electron diffraction (PED) under a scanning PED (SPED) condition. The strain was calculated by the lattice distortion extracted from the PED patterns by a geometric phase analysis algorithm [17, 18]. A reference PED pattern away from the pore and grain boundary was designated as the strain baseline.

Irradiation-induced defects (voids and dislocation loops) in the wrought 316L and AM-316L were characterized by TEM to determine the swelling rate under proton irradiation. The TEM micrographs for void quantifications were taken at an under-focusing image condition with a defocusing value of 1.5µm. The thickness of the specimens was measured with electron energy loss spectroscopy (EELS). Swelling rate (S) was calculated by the equation $S = {}^{V_v}/_{V_t - V_v}$, where V_t is the total volume of sample and V_v is the volume of voids. The Frank dislocation loop was characterized by relrod method [12]. Frank loop preferentially has **{111}** habit planes with a Burgers vector of **a/3<111>**. The required diffraction condition can be obtained by tilting the sample close to the **g = <311>** two-beam condition under the zone axis of **[011]**. One of the four Frank loop variants can be acquired by selecting the relrod streak between **[111]** and **[200]** diffraction spots with the objective aperture. Void size, number density, and dislocation loop size were measured by the line tool in ImageJ, a Java-based image processing program developed at the National Institutes of Health.

Energy-disperse x-ray spectroscopy (EDS) was conducted on 1.80 dpa proton irradiated AM-316L sample in a FEI Talos TEM to investigate composition change after irradiation. Bright-field (BF) and dark-field (DF) TEM micrographs of the radiation-induced voids were taken. Chemical analysis was based on the bulk composition obtained by ICP and LECO methods in Table 1 to avoid contamination information. EDS maps closed to the voids were used to study the radiation-induced segregation in AM-316L SS.

Table 1 Chemical composition (wt%) of wrought 316L and AM-316L SSs analyzed by ICP and LECO.

	C	**Mn**	**P**	**S**	**Si**	**Cr**	**Ni**	**Mo**	**Cu**	**Fe**
Wrought 316L	0.017	1.30	0.031	<0.005	0.41	16.86	10.11	2.00	0.33	Bal.
AM-316L	0.025	0.31	<0.010	0.011	0.73	16.23	13.07	2.09	0.03	Bal.

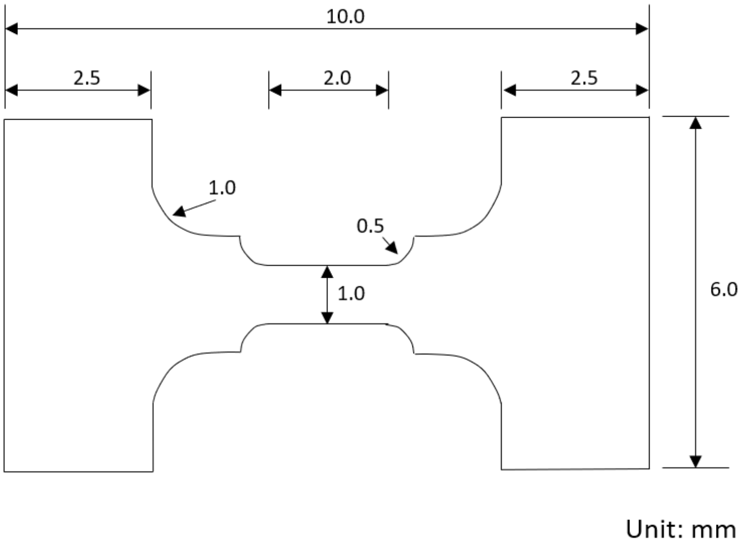

Figure 22 The dimension of *in situ* tensile specimen.

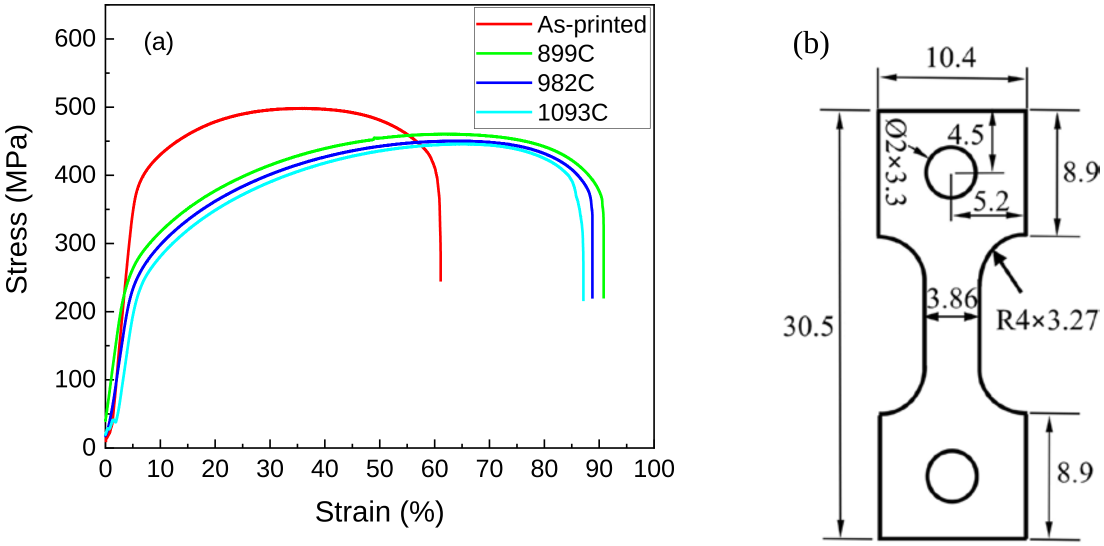

Figure 23 (a) Comparison of AM-316L SS stress-strain curve of as-manufactured and after annealing at 899°C, 893°C, and 1093°C for 45 mins. (b) Tensile specimen dimension in mm, with the thickness of 1.6 mm. Images adapted from Zhang et al., 2020 [20].

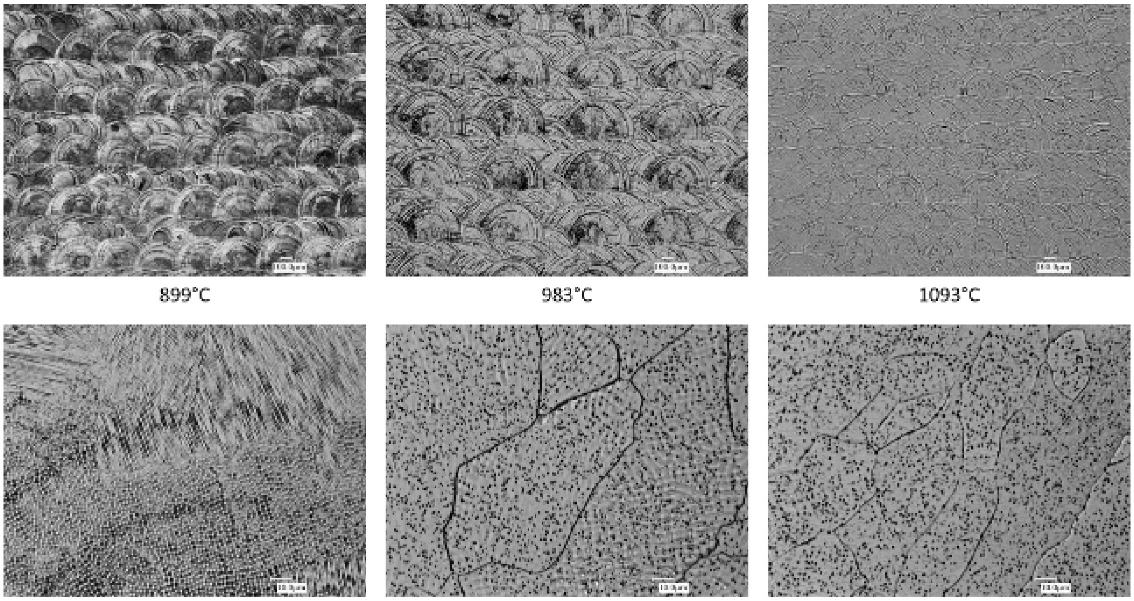

899°C 983°C 1093°C

899°C 983°C 1093°C

Figure 24 Optical micrographs of sub-grain structure after annealing at 899°C, 893°C, and 1093°C for 45 mins. Images reprinted from Zhang et al., 2020 [20].

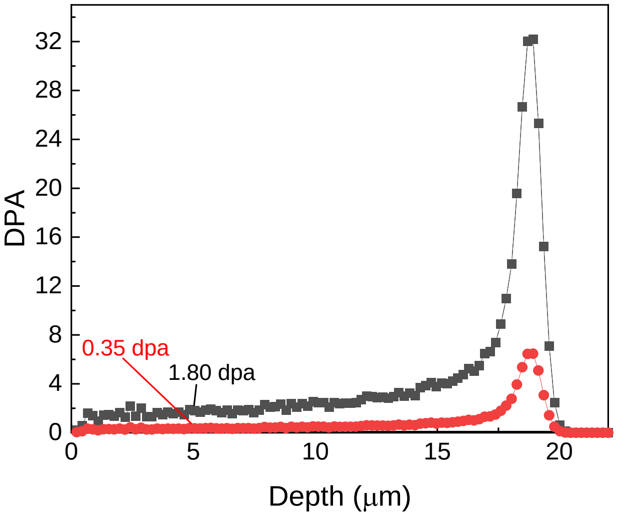

Figure 25 SRIM dpa distribution of 2 MeV proton into 316L SS with 1.80 dpa and 0.35 dpa at a depth of 5μm.

3.2 Results

3.2.1 Microstructure

The morphology of the 316L SS powders used in this study is shown in Figure 26a. The powders exhibited a spherical shape with an average diameter of ~ 20 µm, as seen in the statistical distribution of powder size in Figure 26b. The microstructure of the as-manufactured AM-316L in Figure 26c shows the sub-grains in dendritic and cellular morphology. Pores structures were also observed in Figure 26c. The pores were observed both at the sub-grain boundary and interior of the sub-grains. The pore size distribution in Figure 26d gives an average pore diameter of ~ 200 nm. Figure 27 shows the XRD spectra of the 316L powders and the AM-316L SS, and both 316L powders and AM-316L SS exhibited austenitic phase without evidence of secondary phases. The fitting R_{wp} for 316L powder and as-manufactured AM-316L are 4.82% and 6.99%, respectively. Optical microscopy images in Figure 28a-b present the laser-tracks on the vertical and horizontal surfaces of the AM-316L SS. Figure 28c-d shows the orientation imaging microscopy (OIM) of the AM-316L SS. The grain morphology was highly dependent on the printing orientation. On the vertical surface, Figure 28c, the grain boundary did not fully follow the melt pool boundary, while on the horizontal surface, Figure 28d, the grain morphology followed the laser track and form a V-shape boundary. The distribution of grain orientation in AM-316L was related to the printing orientation. The grain orientation on the vertical surface tended to follow **(111)** and **(101),** and most grains on the horizontal surface were aligned with **(001)**, as seen in the inverse pole figure in Figure 28c and Figure 28d. Both grain morphology and the preferred grain orientation could lead to the anisotropic mechanical properties of the AM-316L. The phase mapping of an area in Figure 28d implies the formation of the body-centered cubic (BCC) delta-ferrite phase in the face-centered cubic (FCC) structured austenite matrix, while the volume percentage of the ferrite phase was too low to be detected by XRD, as seen in Figure 27. Delta-ferrite has been reported in the DED 316L SS and predicted by the Schaeffler and pseudo-binary diagrams [23].

Pores with diameters smaller than 100 nm in the AM-316L SS were characterized in TEM, Figure 29a. Bright-field TEM micrographs of the pore structures, Figure 29b, revealed that the pores exhibited a core-shell structure. The core-shell structure was distinguished by inner and outer interfaces and shared the same orientation with the matrix. High-resolution TEM (HRTEM) micrographs of the inner interface, Figure 29c, and outer interface, Figure 29d, were taken under the zone axis **[001]**. In the lattice strain mapping, Figure 30, the core-shell structure exhibited localized tensile strain. The lattice strain mapping calculated from **(020)**, ε_{xx}, and **(200)**, ε_{yy}, planes were converted to Cartesian coordinates and are shown in Figure 30a and Figure 30b, respectively. The core-shell structure of the pores exhibits a significant tensile lattice strain around ~ 0.4%.

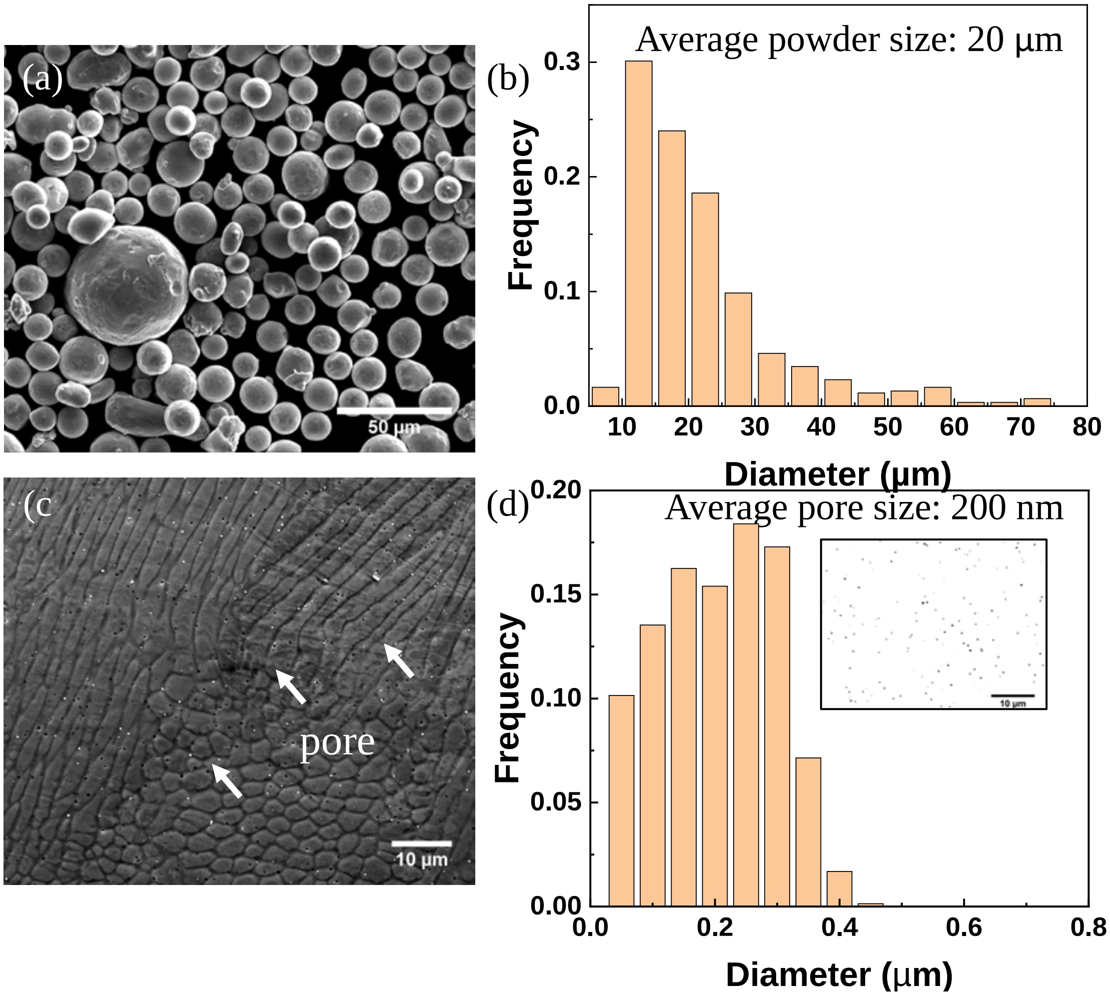

Figure 26 (a) SEM secondary electron micrograph of 316L SS powders. (b) The distribution of powder size showing that the average powder size is 20 µm. (c) SEM secondary electron micrograph of AM-316L SS with pores, showing dendritic and cellular sub-grain structures. (d) Distribution of pore size, showing that the average pore size was 200 nm. The inset image shows the distribution of pore.

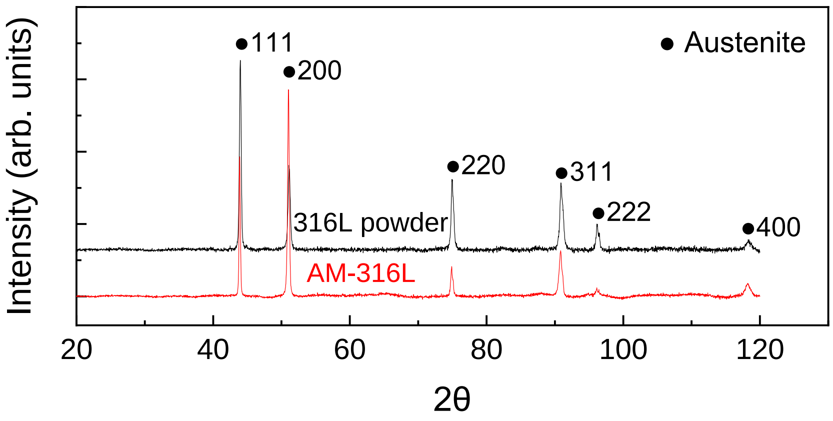

Figure 27 XRD spectra of 316L SS powders and AM-316L SS printed specimen using Cu Kα radiation, showing that austenite was the major phase component identified in both specimens.

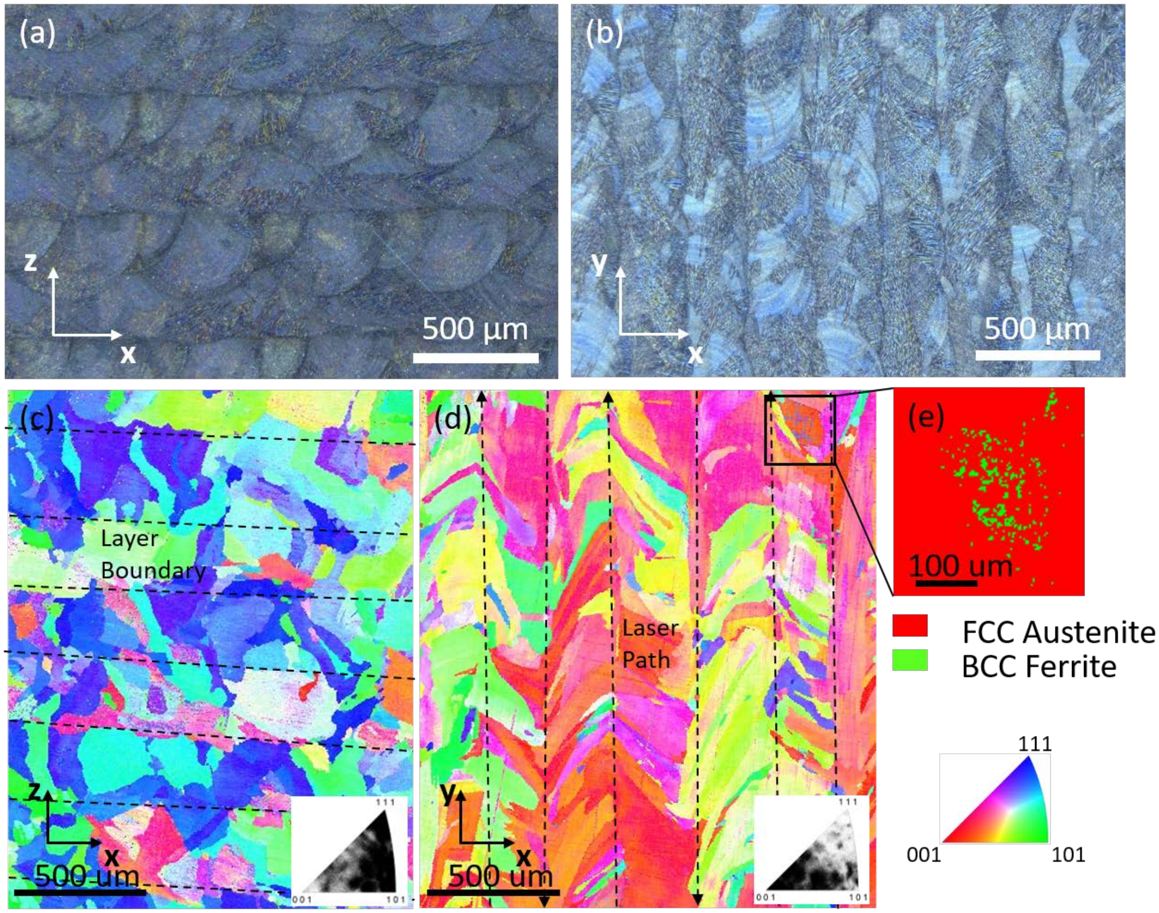

Figure 28 Optical microscopy images of AM-316L SS on (a) vertical and (b) horizontal surface orientation. The orientation imaging microscopy (OIM) of the (c) vertical and (d) horizontal surface orientations reveals the layer structure and laser path.

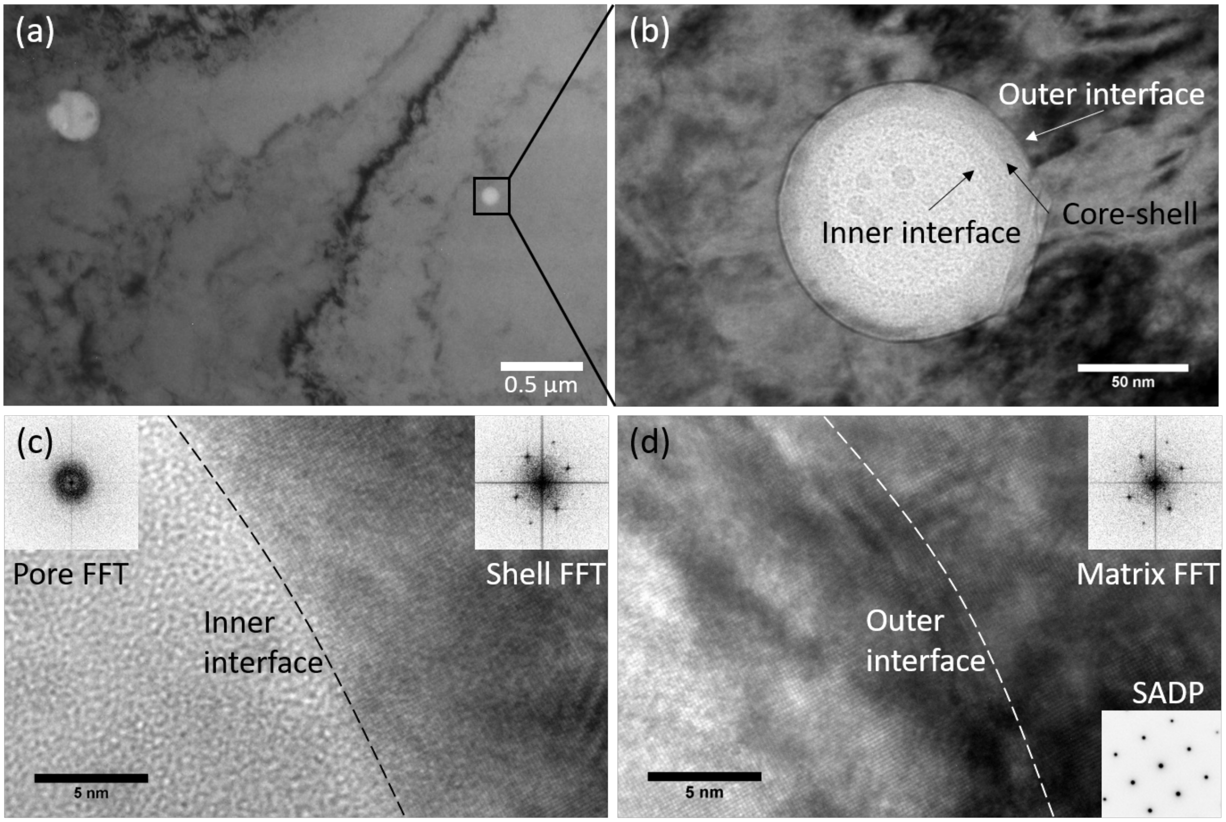

Figure 29 (a) Bright-field TEM micrograph of AM 316L SS, showing two individual pores. (b) Pore exhibited a core-shell structure. (c) High-resolution TEM micrograph of the inner interface of the core-shell structure at the zone axis [001]. (d) High-resolution TEM micrograph of the outer interface of the core-shell structure at zone axis [001].

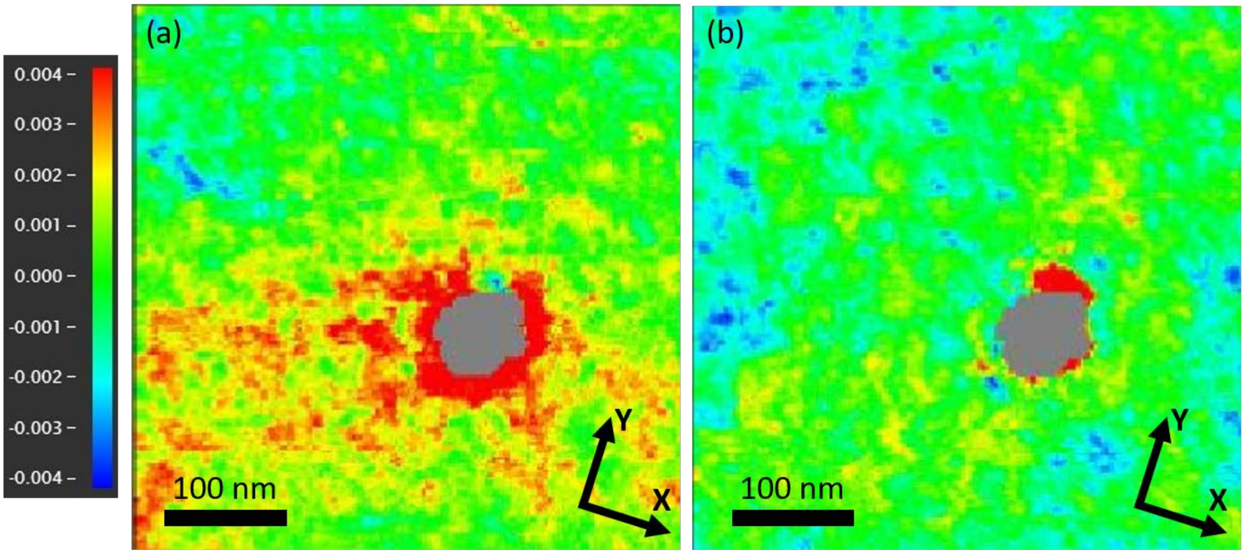

Figure 30 Lattice strain mapping of a pore structure in AM-316L SS. (a) ε_{xx} strain distribution (b) ε_{yy} strain distribution.

3.2.2 Mechanical Properties

Figure 31 shows the tensile properties of the wrought 316L, AM-316Lv, and AM-316Lp at room temperature. The yield strength and ultimate tensile strength are listed in Table 2. AM-316Lv showed the largest yield strength, while the wrought 316L showed the largest ultimate tensile strength. AM-316L exhibited anisotropic mechanical properties, which could be attributed to the formation of the layer structure, laser path, and the preference of grain orientation. Although the average grain size of AM-316L (~250 µm) was larger than wrought 316L (~20 um), as shown in Figure 32, the sub-grain structures, pores, and precipitates could strengthen AM-316L. The porosity in AM-316L could lower the strain-hardening rate, thereby decreasing the ultimate tensile strength and strain-to-failure. SEM micrographs of the fracture surface are displayed in Figure 33, where larger dimples are observed in the wrought 316L than in the AM-316L specimens.

The SEM secondary electron micrographs from *in situ* tensile tests at room temperature with different strain levels are displayed in Figure 34. Large-scale surface roughening and slip bands were observed on the surface of AM-316L during the tensile test. The deformation of AM-316Lp tended to follow the V-shape grain boundary revealed in the EBSD map in Figure 24d. The evolution of grain morphology was more complicated in AM-316Lv than AM-316Lp during the tensile test as the change of grain morphology did not fully follow the melt pool boundary. The evolution of the grain morphology in AM-316Lv implies strong bonding between deposition layers, which led to higher yield strength than AM-316Lp. The orientation and phase mapping of AM-316L after the tensile test is shown in Figure 35. PEDs were collected from the deformed specimens under the SPED mode in TEM. In Figure 35a and Figure 35b, the virtual bright-field image and orientation map clearly show the deformation twins in the microstructure. Interestingly, martensitic phase transformation preferentially occurred in the vicinity of the pores as shown by the phase mapping in Figure 35c. Diffraction patterns of austenite and martensite are shown in Figure 35d and Figure 35e. BCC ferrite was chosen to represent α' martensite in analyzing software due to the low carbon composition of 316LSS.

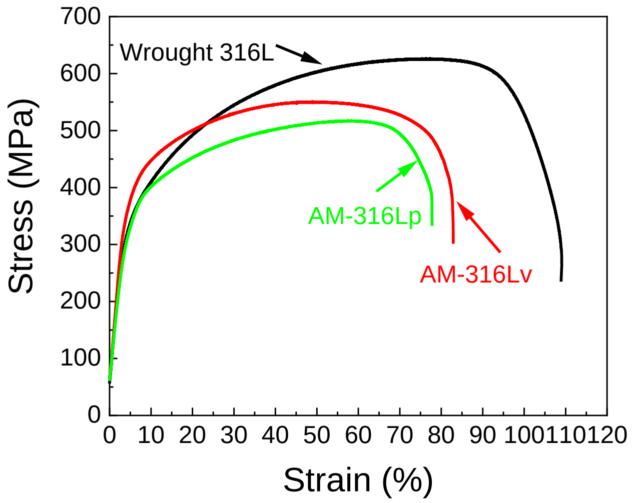

Figure 31 Stress-strain curve of wrought 316L, AM-316Lv, and AM-316Lp. AM-316L has an apparent orientation effect.

Table 2 Yield strength and ultimate tensile strength of wrought 316L, AM-316Lv, and AM-316Lp stainless steel.

	Wrought 316L	**AM-316Lv**	**AM-316Lp**
Yield Strength (MPa)	313 ± 10	370 ± 25	314 ± 17
Ultimate Tensile Strength (MPa)	624 ± 14	561 ± 32	539 ± 14

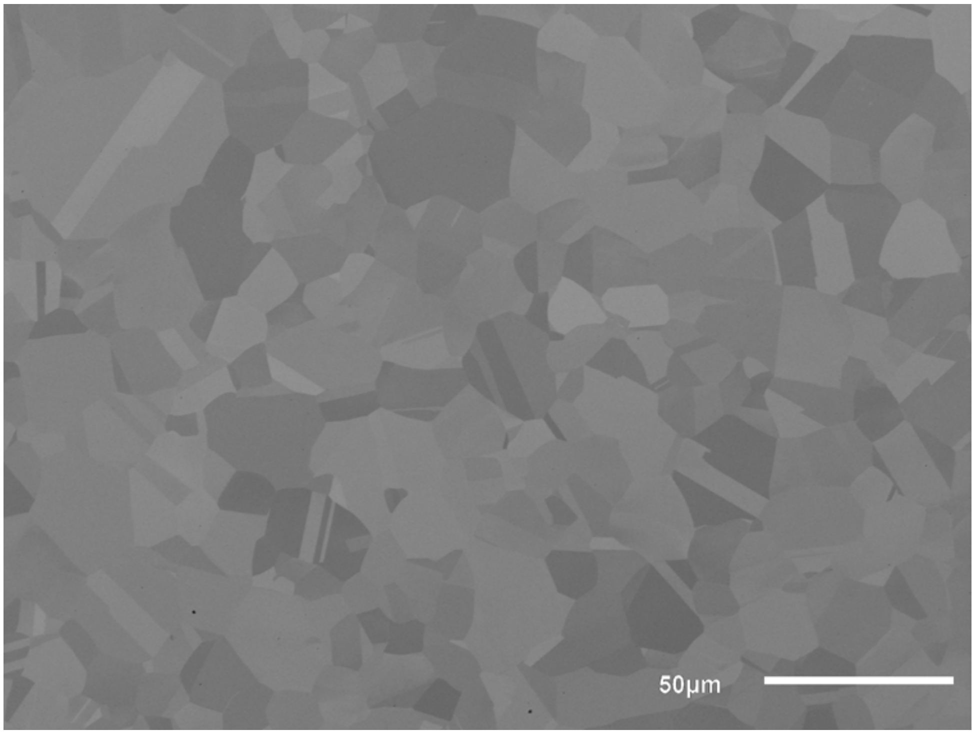

Figure 32 SEM micrograph of electropolished wrought 316L, showing the grain size was about 20 µm.

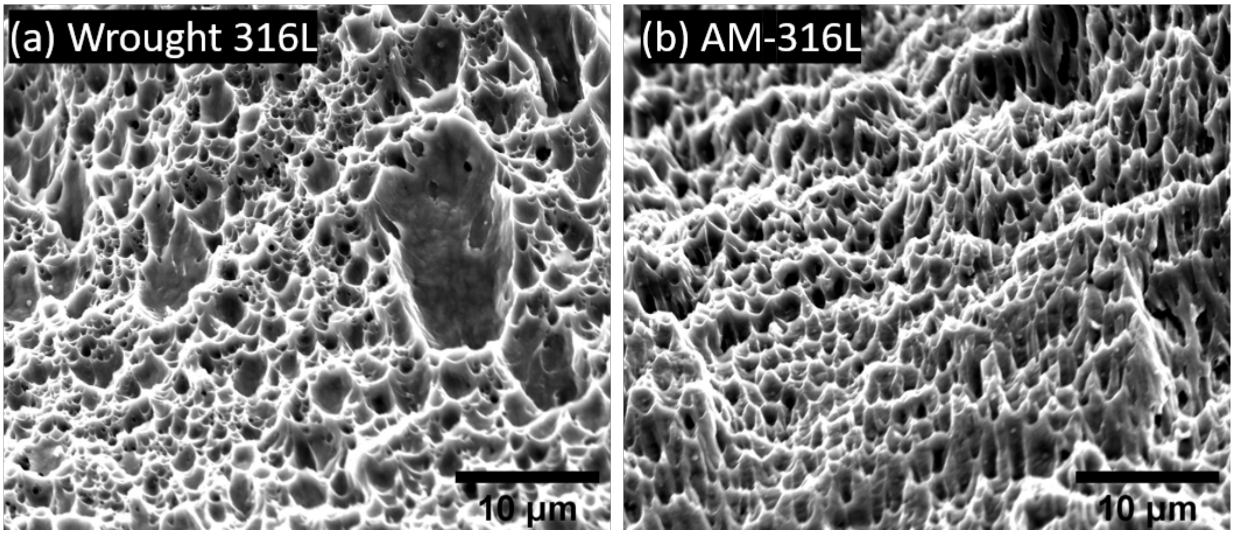

Figure 33 SEM micrographs of (a) wrought 316L and (b) AM-316L fracture surface.

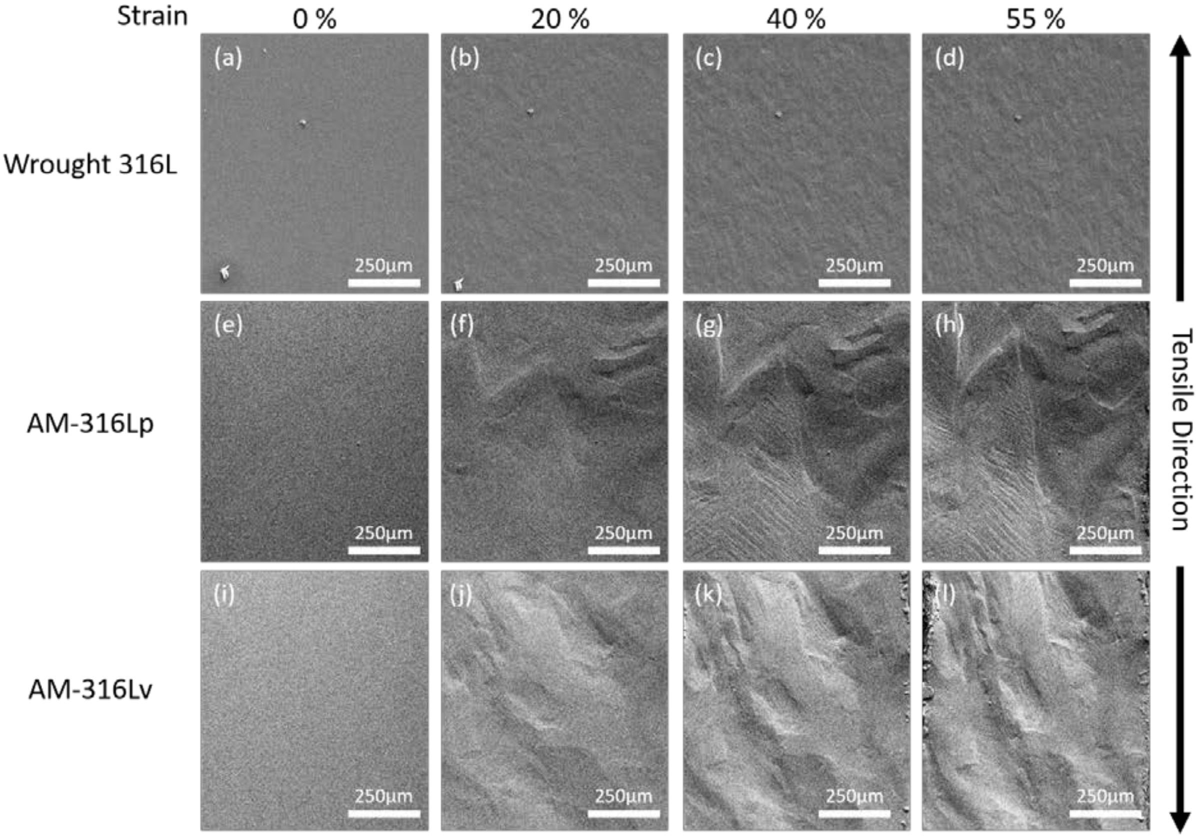

Figure 34 ***In situ*** **tensile test of wrought and AM-316L stainless steels at room temperature in SEM, showing secondary electron micrographs of wrought 316L, AM-316Lp, and AM-316Lv at the strain levels of 0%, 20%, 40%, and 55%, showing the surface roughening in AM-316L.**

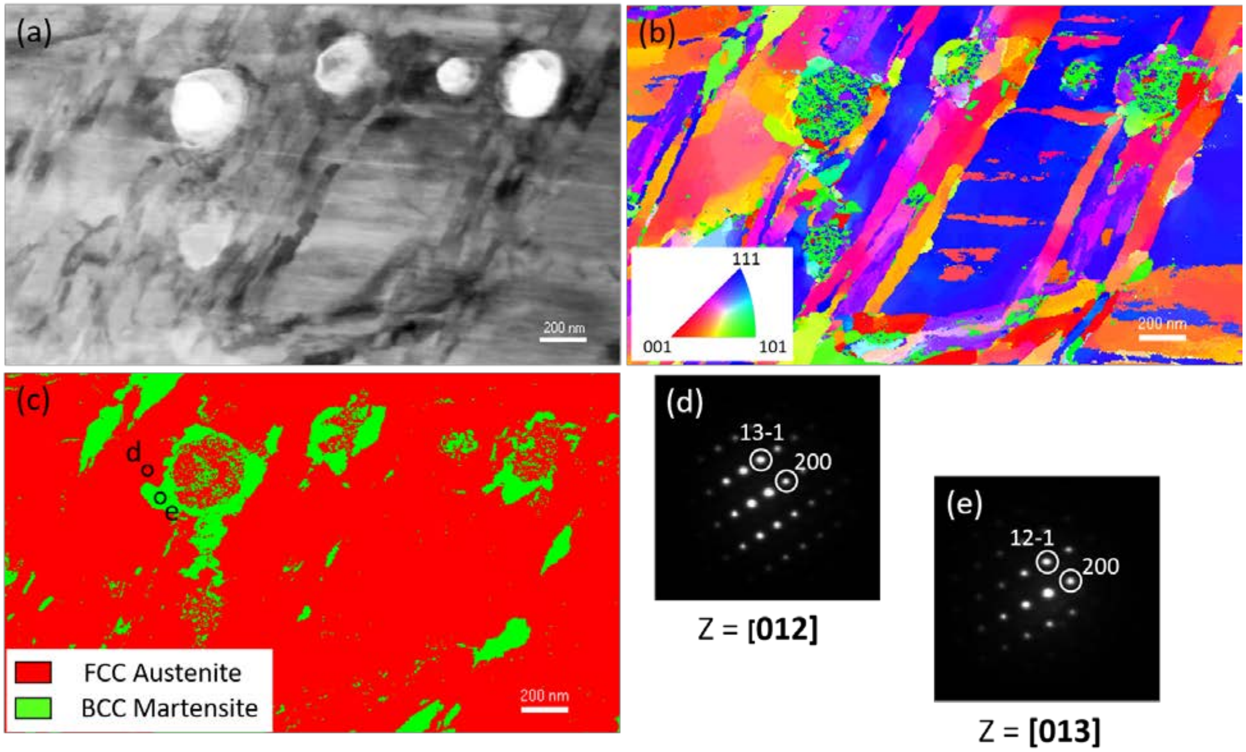

Figure 35 Microstructure of deformed AM-316L SS with pores. (a) ASTAR virtual bright-field. Deformation-induced twins are observed. (b) Orientation mapping of a deformed specimen based on beam direction with positive direction towards the observer. (c) Phase mapping of a deformed specimen. (d) Electron diffraction pattern of region d in (c) showing an FCC structure at the zone axis of [012]**. (e) Electron diffraction pattern of region e in (c) showing a BCC structure at the zone axis of** [013]**.**

3.2.3 Irradiation Damage

The bright-field TEM micrographs in Figure 36 show the evolution of microstructure in the wrought 316L and AM-316L under proton irradiation at 0.35 and 1.80 dpa. Voids formed in both wrought and AM-316L specimens. The void size distribution is shown in Figure 38a. In both wrought and AM-316L, the average void size at 1.80 dpa is larger than that at 0.35 dpa. AM-316L shows a relatively larger void size than wrought 316L, 7.4 nm at 0.35 dpa and 13.9 nm at 1.80 dpa in the AM-316L compared with 5.3 nm at 0.35 dpa and 8.3 nm at 1.80 dpa in the wrought 316L. However, the void density in AM-316L was much lower than that in its wrought counterpart, around one tenth of the void density in wrought 316L. The measurements of the irradiation-induced voids and swelling rate are summarized in Table 3. Swelling rate is compared with other 316L proton irradiation studies in Figure 39 [24-26]. The dpa value from the literature was recalculated with Kinchin-Pease method. The plot indicates the swelling resistance of the DED fabricated 316L in this study could be improved further with proper post heat treatment. It has been reported that the swelling rate of PBF fabricated 316L was reduced with subsequent hot-isotropic pressing [24].

Dislocation loop is another type of irradiation defect in FCC alloys that have been intensively characterized by in austenitic stainless steels [12, 27, 28]. Dark-field TEM micrographs in Figure 37 show the Frank loop distribution in the wrought and AM-316L at 0.35 and 1.8 dpa. Loop size distribution is plotted in Figure 38b, where dislocation loops with size larger than 5 nm were counted. The statistical results of the dislocation loops in Table 3 show that the loop size distribution was very similar in the wrought and AM-316L specimens, while the loop number density in the wrought 316L was larger than that in the AM-316L. This suggests that AM-316L shows a stronger irradiation resistance to the formation of dislocation loops compared to the wrought 316L.

3.2.4 Radiation-induced Segregation (RIS)

EDS results of 1.80 dpa proton irradiated AM-316L are displayed in Figure 40, showing bright-field (BF) and dark filed (DF) TEM micrographs and Fe, Cr, Ni, and Si composition profiles. The EDS maps have shown noticeable RIS around voids and the matrix. An arrow in BF micrograph indicates a void. Ni and Si were found enriched close to the voids and form a specific pattern in the matrix. Voids act as defect sinks, the net flux of vacancies and interstitials diffuse toward it. The undersize solute in austenite, Ni and Si, tend to interact with interstitials and enrich at defect sinks [29, 30]. The enrichment pattern in the matrix could result from dislocations, as dislocations serve as defect sinks and prefer to attract interstitials to release strain. The depletion of Fe was the result of compensating for the enrichment of Ni and Si. Cr is an oversize solute in austenite. The vacancy flux led to the depletion of Cr close to voids and dislocation.

Table 3 Defect size and density in proton irradiated wrought and AM-316L SS.

		0.35 dpa			1.80 dpa		
		Size (nm)	Density ($\times 10^{21}/m^3$)	Swelling (%)	Size (nm)	Density ($\times 10^{21}/m^3$)	Swelling (%)
Wrought 316L	Voids	5.3 ± 1.4	11.13 ± 0.88	0.10 ± 0.01	8.3 ± 2.5	15.88 ± 3.14	0.60 ± 0.11
	Loops	22 ± 10	1.24 ± 0.10	-	21 ± 10	2.11 ± 0.38	-
AM-316L	Voids	7.4 ± 1.9	1.67 ± 0.38	0.04 ± 0.01	13.9 ± 3.8	0.95 ± 0.31	0.16 ± 0.05
	Loops	25 ± 11	1.09 ± 0.24	-	25 ± 12	1.33 ± 0.43	-

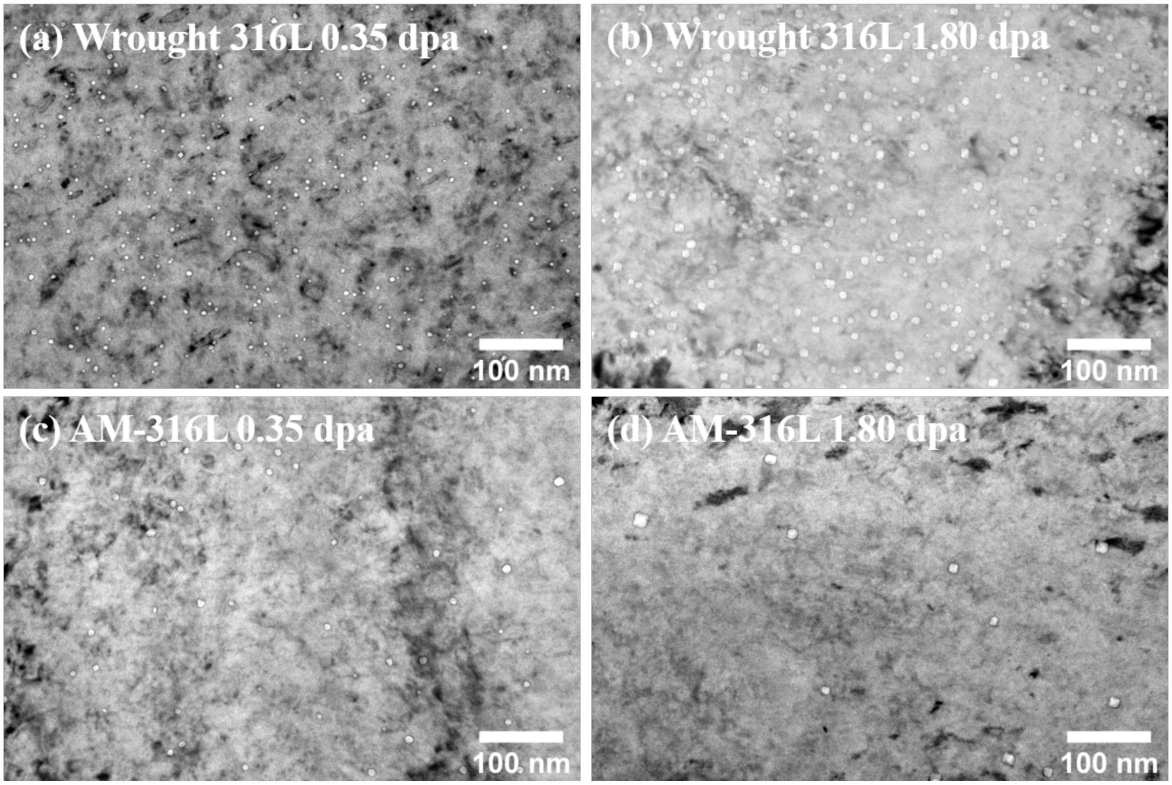

Figure 36 Bright-field TEM micrographs showing voids from proton irradiation. (a) Wrought 316L 0.35 dpa. (b) Wrought 316L 1.80 dpa. (c) AM-316L 0.35 dpa. (d) AM-316L 1.80 dpa.

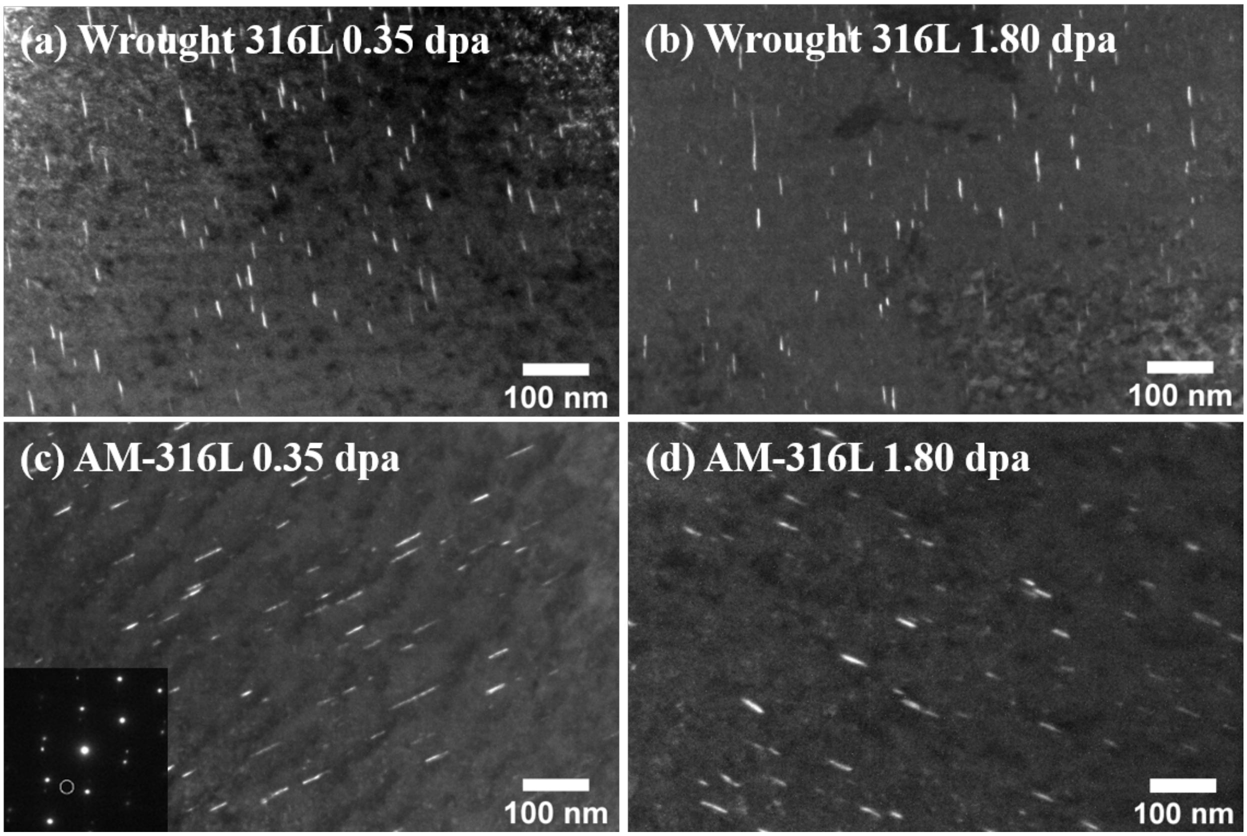

Figure 37 Dark-field TEM micrographs showing Frank loops imaged with the relrod technique after proton irradiation at the zone axis of [011]. (a) Wrought 316L 0.35 dpa. (b) Wrought 316L 1.80 dpa. (c) AM-316L 0.35 dpa. (d) AM-316L 1.80 dpa.

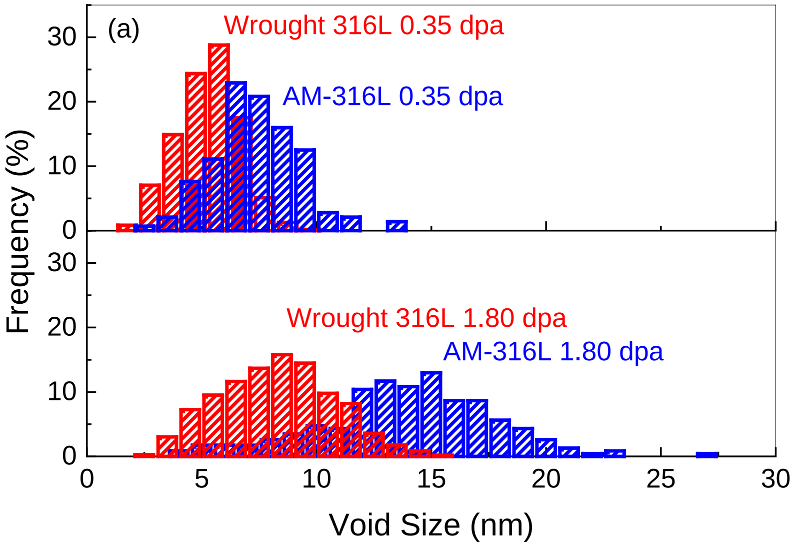

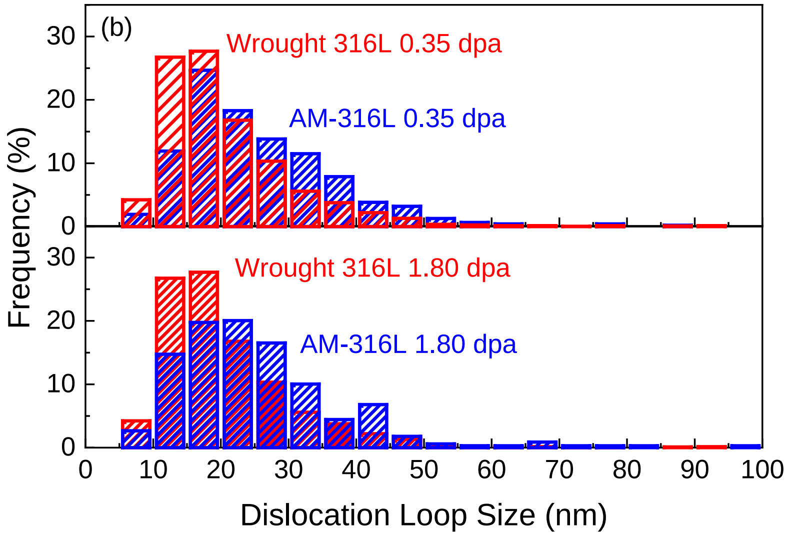

Figure 38 Distribution of voids and dislocation loops in proton irradiated wrought and AM- 316L SS. (a) Void size distribution at 0.35 and 1.80 dpa. (b) Dislocation loop size distribution at 0.35 and 1.80 dpa.

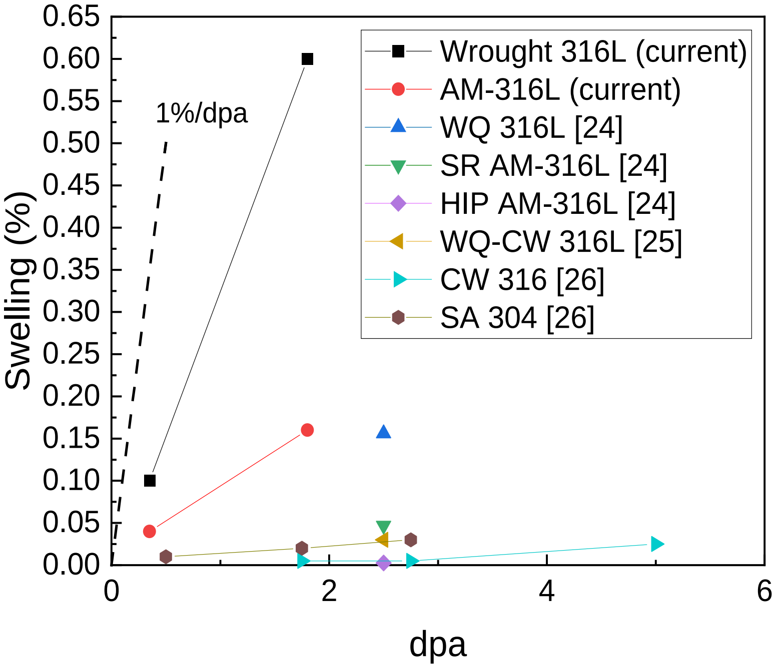

Figure 39 Comparison of AM-316L and wrought 316L proton irradiation swelling rate of current research to published data with different processing. WQ: water quenching, SR: stress relief annealing, HIP: hot-isotropic pressing, CW: cold worked, SA: solution annealing.

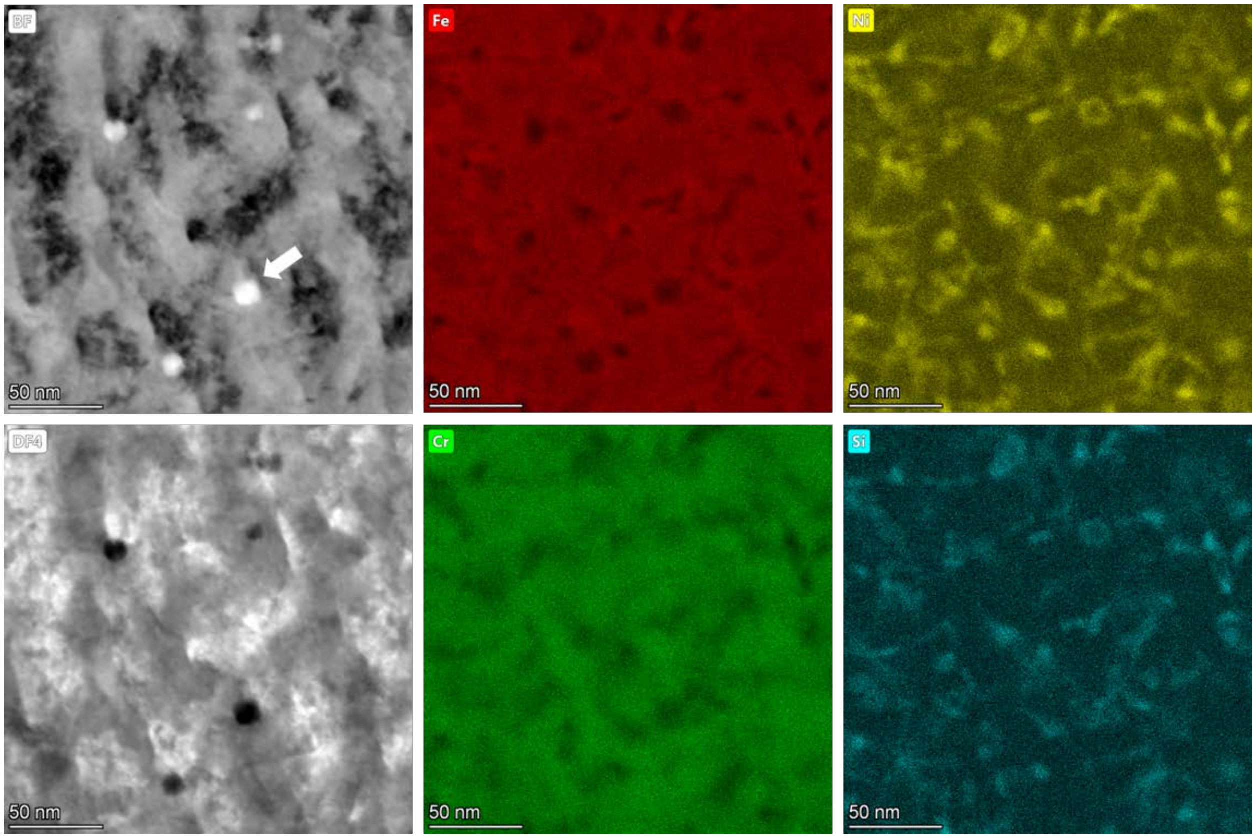

Figure 40 Composition profile obtained from EDS in TEM after proton irradiation, showing BF and DF TEM micrographs with the composition profile of Fe, Cr, Ni, and Si. The arrow in BF micrograph indicates a void.

3.3 Discussion

Deformation-induced martensitic phase transformations could increase strain hardening rate and, therefore, the stain-to-failure [31]. In this study, deformation-induced α' martensite was preferentially located around pores with localized tensile strain fields. The localized tensile strain was possibly the result of the high cooling rate around the pore. Manikandan et al. [32] reported that lattice parameter and cooling rate positively correlate in a comprehensive study on how cooling rate affects the microstructure of Inconel. The high cooling rates trap the solute in the region and expand the lattice parameter to create a localized tensile-strain field around the pore. The fabrication-induced nano-voids promotes the martensitic phase transformation in AM-316L. Javanbaknt et al. [33] proposed a phase-field model to analyze the evolution of strain-induced martensitic transformation. The model predicted nanovoids to increase the rate of phase transformation during deformation. The stress concentration around the nanovoid can activate the phase transformation with a lower strain than solid material. The study provided direct evidence that the nanopores in the material facilitated the transformation of the martensitic phase.

Pham et al. [34] reported that the twinning-induced plasticity (TWIP) behavior contributes surprisingly good tensile ductility in AM 316L SS. The TWIP behavior was attributed to the nitrogen solute atoms as nitrogen reduces the stacking fault energy of austenitic stainless steels. In this study, deformation twinning occurs in AM 316L SS after tensile tests at room temperature. In Figure 34, the ladder-like structure from twinning was found over the surface of the sample. The orientation mapping of AM-316L showed the deformation twin network developed after tensile testing, as seen in Figure 35b. The sub-grain structure and chemical segregation possess a significant influence on the deformation mechanism of AM alloys. Wang et al. [35] concluded that the chemical segregation along the sub-grain cellular boundary could pin down dislocations and promote twinning. Han et al. [36] reported that the existence of nanovoids could block the propagation of dislocation slip and activate deformation twinning. The deformation mechanism of AM alloys can be tailored by controlling the microstructure by adjusting printing parameters.

Radiation damage has been proved to facilitate deformation-induced martensitic transformation in austenitic steel [37-39]. Kadyrzhanov and Maksimkin [40] concluded that the critical strain to initiate martensitic transformation decreases as the neutron fluence increases. Dislocation loop and point defects introduced from irradiation provide the driving force for phase transformations. Here it was found that AM-316L had a lower swelling rate and dislocation loop density than wrought 316L. Sub-grain boundaries have been proved to be defect sinks [41]. Another possible mechanism is that pores could serve as defect sinks to capture the irradiation defects. The free surface was an effective defect sink in nanoporous Au and Ag during irradiation [42, 43]. Chen et al. [44] found voids in nanovoid-nanotwinned copper could absorb dislocation loops during *in situ* Kr irradiation.

Moreover, twin boundaries could serve as a diffusion highway to transport interstitials to void, resulting in the shrinkage of void size. In a study from McMurtrey et al. [45], irradiation-assisted stress corrosion cracking (IASCC) in AM-316L was mitigated due to the lower density of radiation defects. The fabrication-induced pores absorbed point defects during irradiation reduced the localization of deformation. This study indicated that the presence of manufacturing-induced features in AM alloys' microstructure could positively impact the irradiation tolerance.

3.4 Conclusion

Microstructure, mechanical properties, and irradiation damage of AM-316L SS fabricated by DED technique were studied. The pore structures formed during printing show a core-shell structure with a tensile lattice strain as large as ~0.4%. The anisotropic mechanical properties of AM-316L could be attributed to the preferred grain orientation and morphology created by the laser track. Deformation-induced martensitic phase transformation and twinning occur in AM-316L SS during the tensile tests at room temperature. The localized lattice strain of the fabrication-induced pore structures promoted the martensitic phase transformation. Under proton irradiation at 360 ºC, the AM-316L showed a lower swelling rate and dislocation-loop density than the wrought 316L SS. The pre-existing sub-grain boundaries and pore structures could potentially serve as defect sinks to capture the defects generated by radiation and thereby mitigating the void swelling.

CHAPTER IV

MICRO-PILLAR COMPRESSION

4.1 Introduction

Microscale mechanical testing based on micron-pillar compression was applied to understand the effect of thermal annealing and ion irradiation on yield strength and resolved critical stress. The mechanical property changes are coupled with microstructural information obtained from TEM to explain the strengthening mechanisms. Pillar compression has the advantage of site selection, making it possible to obtain single crystal grain's mechanical properties without the complexity of grain boundaries. Furthermore, the site selection allows local determination of grain orientations. Therefore, the resolved shear stress can be calculated by the Schmid factor. Such studies are essential to evaluate the effects of defects introduced from additive manufacturing, such as large pores, and the defects from ion irradiation, including nanometer-size voids and dislocation loops. The site selection approach also excludes the effects from grain boundaries. Therefore, the effects from complicated grain morphology are excluded.

4.2 Experimental procedure

Due to the sensitivity of surface quality for EBSD, polishing procedures must be done cautiously. The specimens were mechanically polished, followed by electropolishing in a solution of 15.4% water, 46.1% H_3PO_4, and 38.5% H_2SO_4 with a 4V potential for 13 seconds. This study utilized EBSD to map phases, grain morphology, and orientation.

EBSD is a technique based on Bragg's reflection from inelastically scattered electrons. Inelastically scattered electrons distribute large angles and form a pair of excess and defect lines, which constitute the Kikuchi pattern. By indexing the Kikuchi pattern, the phase and orientation of the materials can be obtained. EBSD can identify smaller features than regular broad beam XRD due to its fine electron beam spot size.

We compared three variants, including as-manufactured, annealed, and irradiated 316L. Mappings were performed mainly along with the vertical printing orientation. Mapping on vertical and parallel orientation were compared. EBSD mapping was performed in Tescan FERA-3 plasma focused ion beam (FIB) chamber. For each pillar, the orientation information was used to calculate the Schmid factor to extract the critical shear stress.

Micro-pillar compression tests were performed on AM-316L, virAM-316L, and 1.80 dpa proton irradiated AM-316L (irrAM-316L) at room temperature. Details of proton irradiation are in the next section. The pillars of virAM-316L were in the unirradiated region in the proton irradiated sample to eliminate the annealing effects from long-hour irradiation. EBSD determined pillar orientation, and the site was preliminarily milled in Tescan FERA-3 plasma FIB. The final pillar dimension was achieved by Tescan Lyra-3 gallium FIB due to the lower etching rate has better control on dimension. Pillar dimension was about 5 µm in diameter and 10 µm in height, as seen in Figure 41. Compression tests were conducted in Hysitron TI-950 Triboindenter with a 20 µm flat-punch tip and high-load transducer. A constant strain rate of 1×10^{-3}/s was applied for the compression tests. Table 4 is the list of sample identifiers used in this article.

Table 4 Identifiers and the conditions of additively manufactured 316L SS samples for pillar compression.

Identifiers	Conditions
AM- 316L	As printed
virAM-316L	Unirradiated region in 983°C annealed, proton irradiated sample
irrAM-316L	983°C annealed and proton irradiated

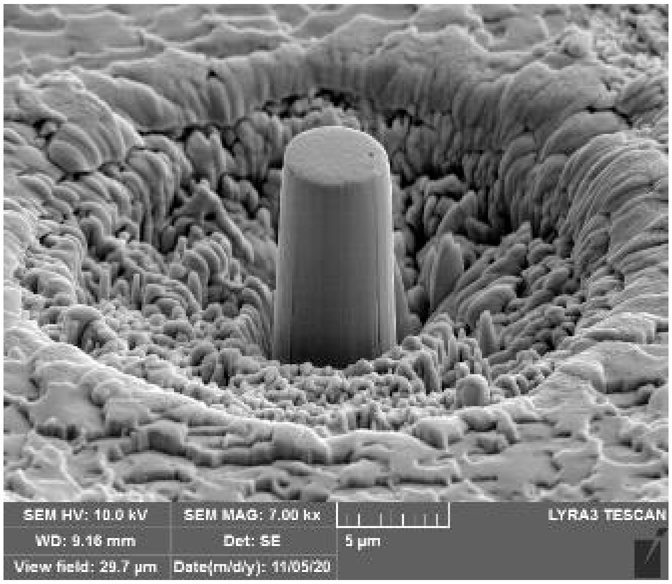

Figure 41 SEM micrograph of micro-pillar.

4.3 Results

Figure 42a shows SEM micrograph of as-manufactured AM-316L where pillars were prepared. Figure 42b shows the corresponding EBSD mapping. The grain size is about 250 µm. The region was selected to include several orientations, and multiple pillars were prepared from the selected orientation. For each variant, grains are selected such that a pillar is made within a single domain to exclude grain boundary effects. Figure 43 and Figure 44 are SEM micrographs and EBSD mapping of annealed and ion irradiated samples, respectively.

Pillar preparation was intentionally selected in relatively large grains to avoid the complexity of a grain boundary. The presence of a grain boundary increases the yield strength due to dislocation blocking by boundaries. As one example, Figure 45 compares the stress-strain curves of two grains, one contains a grain boundary, and the other is boundary-free. Note that both are (245) oriented in EBSD mapping from the top. The effect on compression responses is noticeable. It is worthy to point out a grain boundary is visible under SEM micrograph, Figure 46. Each fabricated pillar was investigated through SEM imaging to verify it was boundary-free. Figure 47a-c compares the pillar compression curves from as-manufactured, annealed, and irradiated samples, respectively. Due to variations in grain orientations, curves exhibit differences in yield strength and load drops. For each curve, the yield strength is measured and used to extract the critical resolved shear stress ($\boldsymbol{\tau_{crss}}$) by using Schmid factor (m) determined from EBSD mapping, according to the equation:

$$\tau_{crss} = \sigma_y cos\lambda cos\phi = \sigma_y m \tag{4.1}$$

where λ represents the angle between load direction and slip plane, and ϕ is the angle between load direction and slip direction.

The load drops, indicated by arrows in Figure 47a-c, correspond to slip activation during compression. As shown in Figure 48a-b, which are from as-manufactured, annealed, and irradiated variants, respectively, multiple slips were observed in SEM imaging of pillars after the compression. Judged by the deformation, all samples exhibit certain ductility. **Table 5** lists the critical resolved shear stress for three variants. First, the average $\boldsymbol{\tau_{crss}}$ is consistent among different variants, judged by the statistic errors. For as-manufactured 316L, the average $\boldsymbol{\tau_{crss}}$ is 106 ± 13 MPa. After annealing for strain relaxation, the average $\boldsymbol{\tau_{crss}}$ is reduced to 87 ± 13 MPa, corresponding to a change of -17.9%. For proton-irradiated 316L, the average $\boldsymbol{\tau_{crss}}$ is increased to 246 ± 25 MPa, corresponding to a change of 182.8% compared to the annealed variant. **Table 5** also lists the measured modulus (E) along different orientations. E along (111) direction, ranging from 162 GPa to 199 GPa, are consistently higher than that from other orientations, which is expected. Figure 49 compares the critical resolved shear stress obtained from three variants. The dot symbols are the results from individual pillars. The error bars represent the standard deviations. The comparisons show that thermal annealing reduced critical resolved shear stress, and ion irradiation significantly increased the stress. The CRSS decreased to the wrought 316L SS region after annealing, which is between 80 MPa to 90 MPa and marked by the red dash line in Figure 49 [46], indicating the residual stress in AM-316L had a more significant impact on mechanical properties.

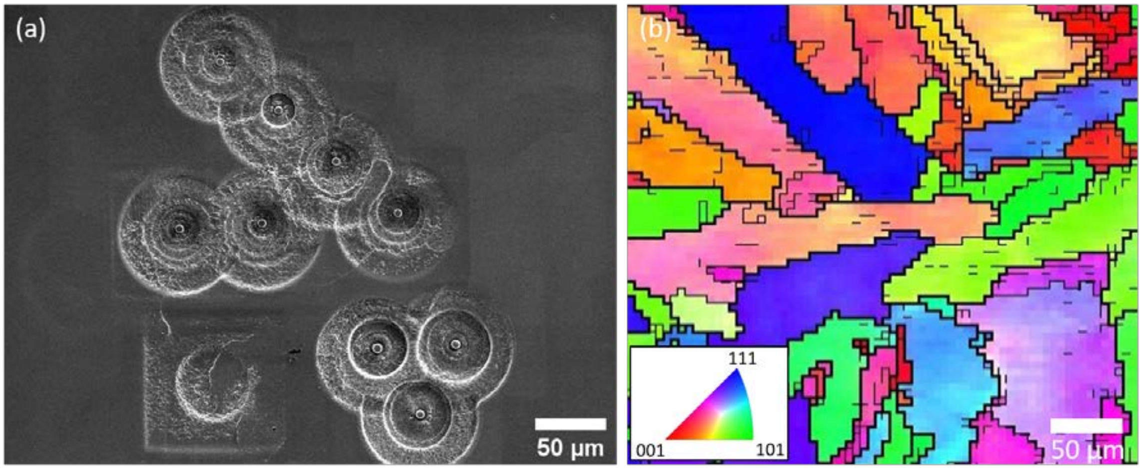

Figure 42 SEM micrograph of pillar location on AM-316L and corresponding EBSD map.

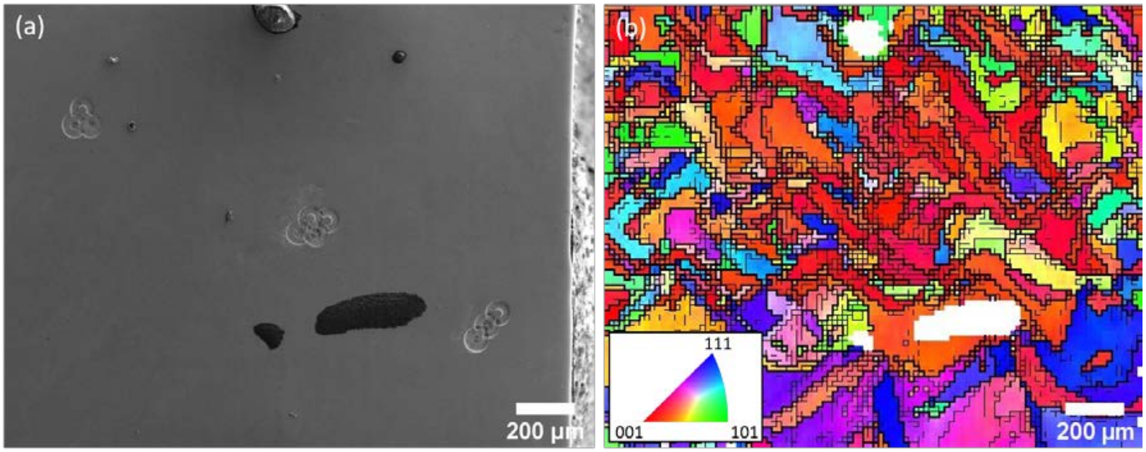

Figure 43 SEM micrograph of pillar location on virAM-316L and corresponding EBSD map.

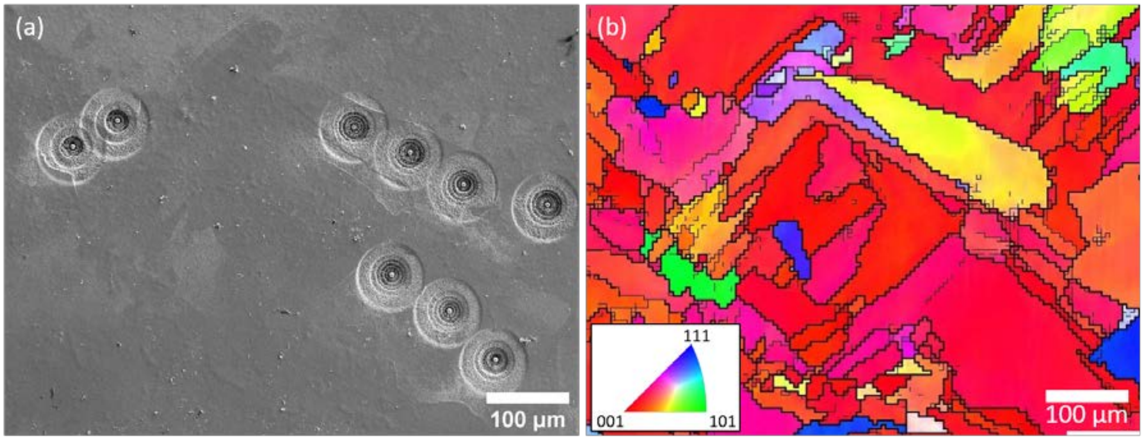

Figure 44 SEM micrograph of pillar location on irrAM-316L and corresponding EBSD map.

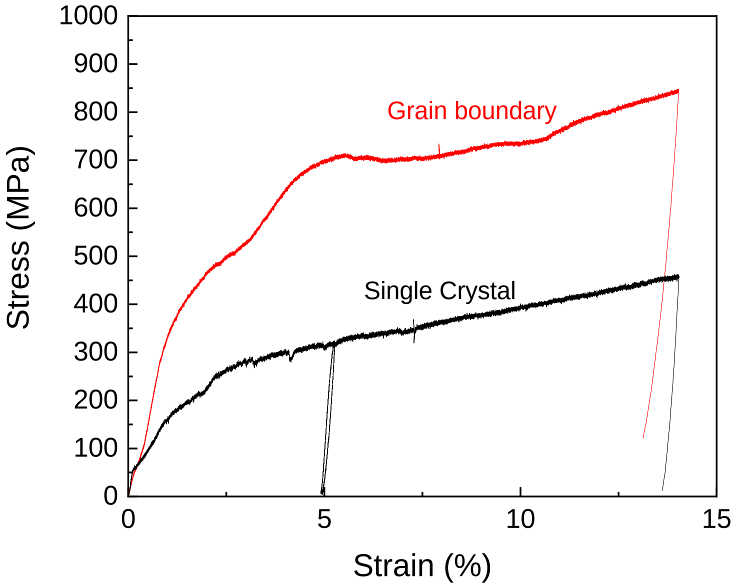

Figure 45 Stress-strain curve comparison between the pillar contained grain boundary and the single crystal pillar in AM-316L at (245) orientation.

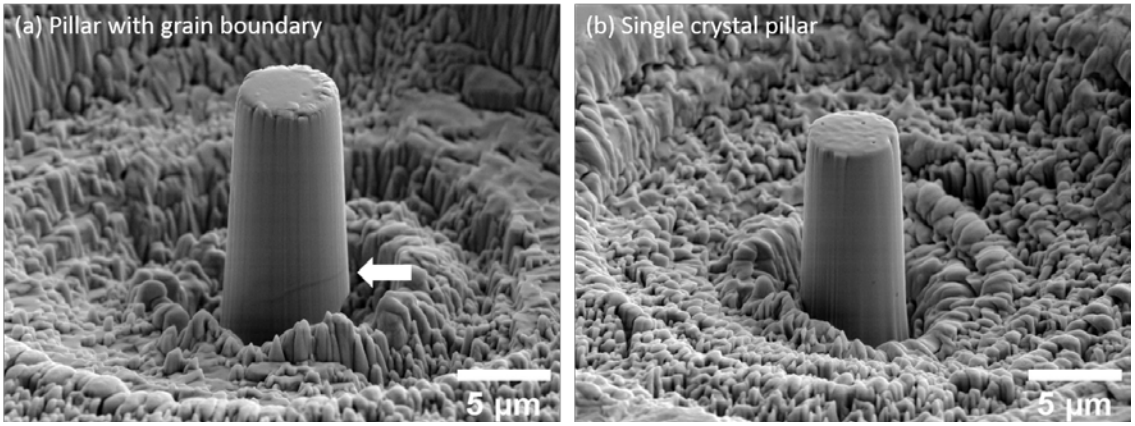

Figure 46 SEM micrographs showing the appearance difference between (a) the pillar contained grain boundary, pointed by the arrow, and (b) the single crystal pillar.

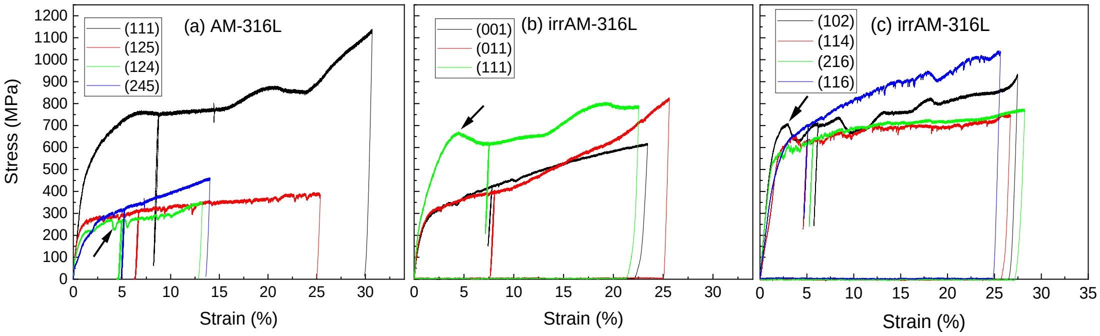

Figure 47 Pillar compression stress-strain curve for various orientations of (a) AM-316L, (b) irrAM-316L, and (c) irrAM-316L, with the arrows indicate the load drops.

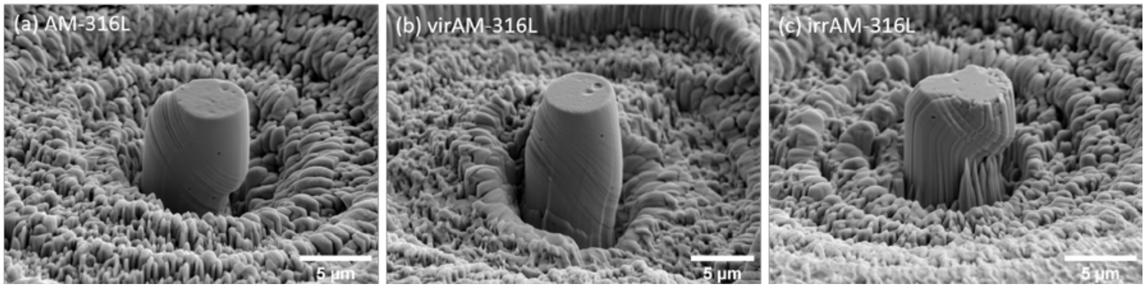

Figure 48 SEM micrographs of compressed pillars of (a) AM-316L, (b) virAM-316L, and (c) irrAM-316L. Dislocation slips were observed in all conditions.

Table 5 Pillar compression results of AM-316L, virAM-316L, and irrAM-316L.

Sample	Orientation	σ (MPa)	E (GPa)	Max. m	τ_{crss} (Mpa)	Average τ_{crss} (MPa)	$\Delta\tau_{crss}$
AM-316L	(125)	200	120	0.49	98	106 ± 13	--
	(125)	197	105.9	0.49	96.53		
	(125)	203	124.4	0.49	99.47		
	(124)	202	100.3	0.49	98.98		
	(245)	198	137	0.44	87.12		
	(111)	461	172.3	0.27	124.47		
	(111)	451	163.8	0.27	121.77		
	(111)	446	199.3	0.27	120.42		
virAM-316L	(001)	176	99.2	0.41	72.16	87 ± 13	-17.9 %
	(001)	232	80.8	0.41	95.12		
	(011)	259	147.3	0.41	106.19		
	(011)	234	124.9	0.41	95.94		
	(111)	316	161.8	0.27	85.32		
	(111)	256	180.7	0.27	69.12		

Table 5 Continued

Sample	Orientation	σ (MPa)	E (GPa)	Max. m	τ_{crss} (Mpa)	Average τ_{crss} (MPa)	$\Delta\tau_{crss}$
irrAM-316L	(102)	542	120.8	0.49	265.58	246 ± 25	182.8 % from virAM-316L
	(102)	510	136.8	0.49	249.9		
	(102)	578	109.3	0.49	283.22		
	(114)	476	106.4	0.45	214.2		
	(114)	588	101.6	0.45	264.6		
	(216)	529	99	0.49	259.21		
	(116)	481	100.8	0.45	216.45		
	(116)	486	92.9	0.45	218.7		

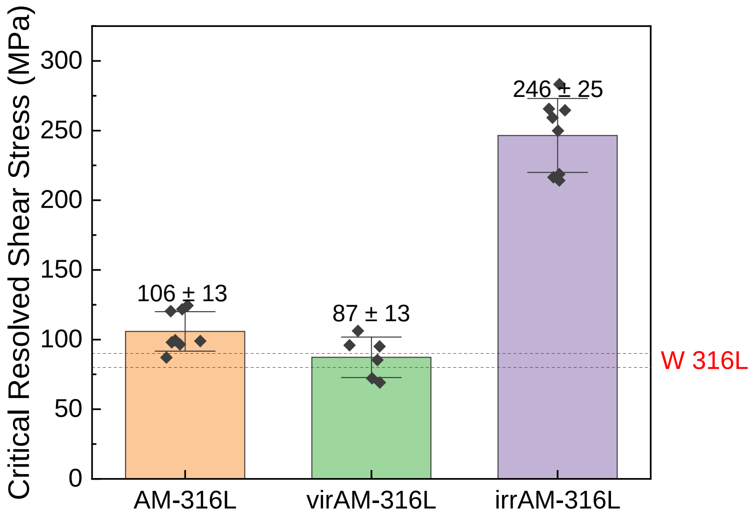

Figure 49 Plot of the critical resolved shear stress for AM-316L, virAM-316L, and irrAM-316L, showing the evolution after heat treatment and proton irradiation.

To shed light on the deformation mechanism, FIB was used to lift specimens from the compressed pillar. Figure 50 shows a typical TEM micrograph from the as-manufactured variant. No grain boundaries and no twinning were observed. The insert in Figure 50a, the localized diffraction patterns, shows a single FCC phase without twinning. No phase transformation is observed. The deformation strain for the investigated AM-316L pillar was about 13%, which might be too low to activate twinning or phase transformation. The white box on the left bottom corner highlights a pore of ~200 nm. Note that similar pores are frequently observed under TEM, and they represent a vital microstructure feature created from additive manufacturing. Pores play an essential role in influencing mechanical properties. As shown in Figure 50b, dislocation bowing occurs around a pore, as marked by the arrow. The pore in the pillar also created a dislocation-concentrated region while interacting with dislocation, as shown in Figure 50b. The strain provided by the high-density dislocation beside the pore could also assist phase transformation.

Figure 51 shows the TEM micrograph in the annealed variant. The pillar was compressed up to 23% strain. More than one phase was observed in the diffraction pattern, as shown in the insert. The new phase was identified as ε martensite, which is most likely induced by the deformation. Both γ austenite and ε martensite are indexed in the diffraction pattern. ε martensite is hexagonal closed-pack (HCP) structure and is a precursor phase to α' martensite. The presence of ε martensite indicated some regions in virAM-316L might underwent twinning during deformation and the possibility to develop α' martensite at higher strain. Figure 52 shows the TEM micrographs of the irradiated 316L pillar, which had about 24% strain. A large area of twinning was found in the specimen. Figure 52c is the twinning diffraction pattern at **z = [011]**, with the lines showing two sets of diffraction patterns.

Voids are observed in the irradiation sample, but they exhibited two different sizes. The large ones having sizes of a few hundred nanometers are created from additive manufacturing, similar to the observation in both as-manufactured and annealed variants. The small ones having sizes of a few nanometers are created by proton ion irradiation. In Figure 52d, twinning was found intercepted by the large pores created from the manufacturing. The pore acted like a pivot point, which stopped the twin from propagating to the other side. Figure 53a-c shows the behavior of radiation-induced small voids under deformation. As shown in Figure 53a, the voids between twins had no sign of deformation and remained their spherical shapes. In comparison, voids within a twin region were deformed and elongated, Figure 53b. Figure 53c shows a void that was cut by the dislocation gliding.

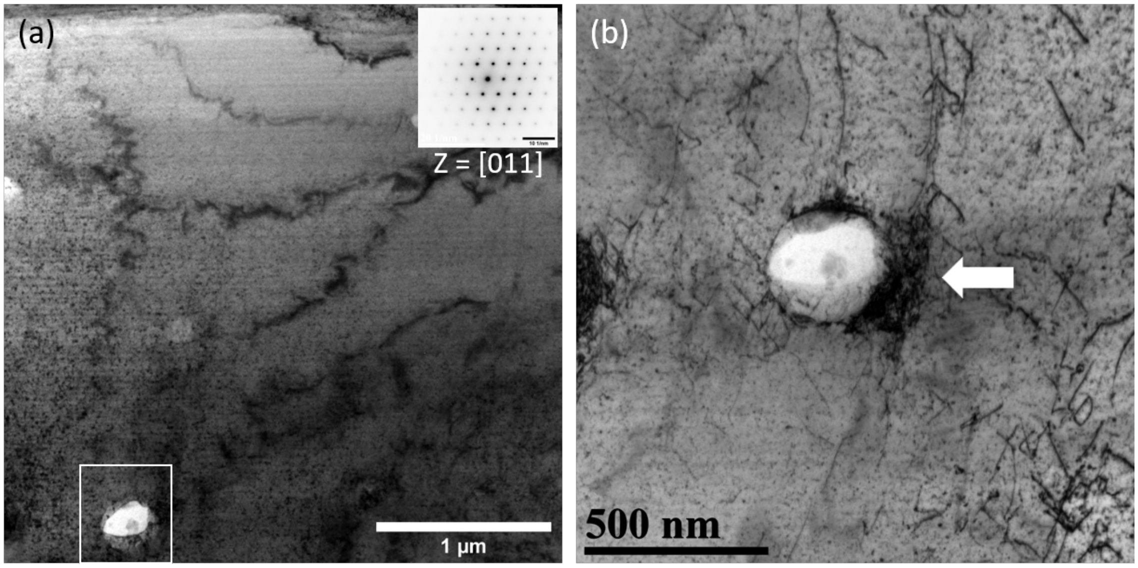

Figure 50 TEM micrographs from AM-316L (124) orientation compressed pillar. (b) showing dislocation bowing while interacting with pore.

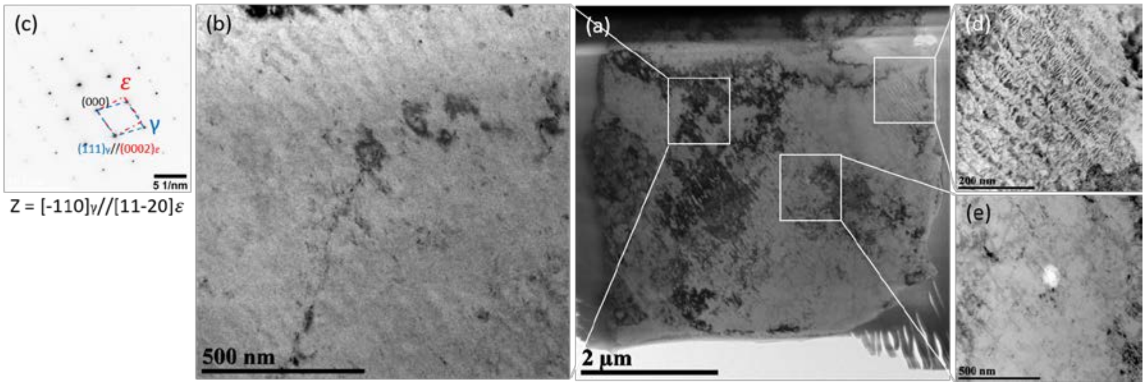

Figure 51 TEM micrographs from virAM-316L (001) orientation compressed pillar. (a) shows the overview of the pillar. (b) shows the region contains ε martensite. (c) is the regional diffraction pattern at z = [-110], showing the presence of ε martensite. (d) shows the dislocation slipping. (e) shows the intersection of slips and pore.

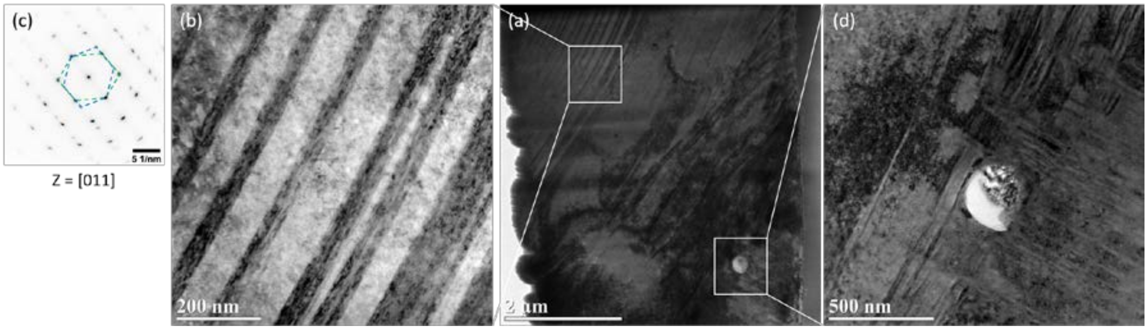

Figure 52 TEM micrographs from irrAM-316L (116) orientation compressed pillar, showing twinning (b) and diffraction pattern (c). (d) shows the intersection of twin and pore.

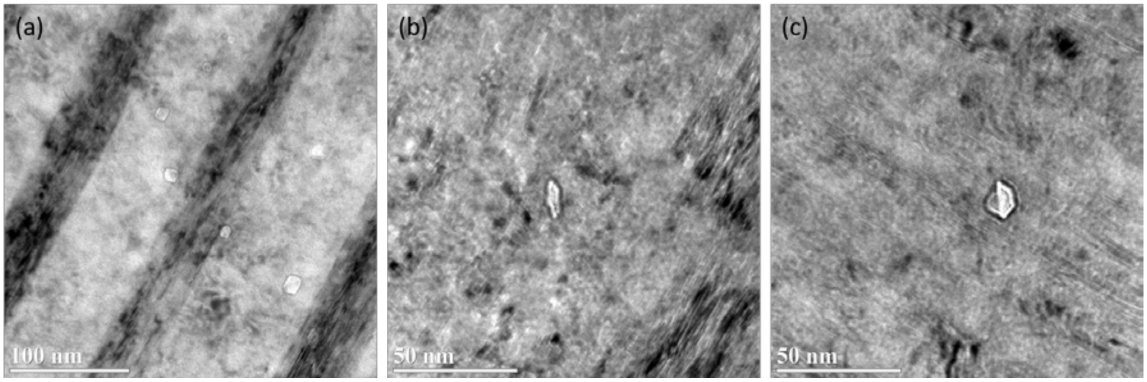

Figure 53 TEM micrographs of irrAM-316L compressed pillar, showing the void behaviors under deformation. (a) Voids in the region between twins remained undeformed. (b) Voids in the twin region were compressed and elongated. (c) Voids were cut by dislocation gliding.

4.4 Discussion

The twinning of irradiated austenitic alloys during deformation has been widely observed [47-51]. Dissociation of dislocation into Shockley partial dislocations plays a vital role in the plastic deformation of austenitic alloys. In austenitic alloys, dissociation happens on the (111) plane from the Burgers vector of $a/2 < 1-10 >$ into $a/6 < 2-1-1 >$ and $a/6 < 1-21 >$. Partial dislocations create two twin boundaries, which alter the mechanical properties and the response to radiation. The separation distance between two partial dislocations depends on stacking fault energy (SFE), the magnitude of the Burgers vector of the perfect dislocation, and the position/angle relative to the external stress field. Dissociation will occur when the external shear stress is greater than the critical shear stress to separate the partial dislocations. The critical shear stress τ_x^{crit} is a function composed of stacking fault energy (SFE) γ_{SF}, and Burgers vector of the perfect dislocation b_p, as given by [52]:

$$\tau_x^{crit} = \frac{2\gamma_{SF}}{b_p} \tag{4.2}$$

Critical shear stress can be achieved by strengthening methods, including irradiation, lowering temperature, and increasing strain/strain rate. Radiation-induced defects, such as voids and dislocation loops, strengthen materials and reach the critical shear stress to form twins. The separation distance between the two Shockley partial dislocation increases as radiation dose increase or at higher SFE. We believed that radiation in the present study significantly enhanced twinning through the above mechanism.

Radiation-induced voids and dislocation loops strengthen the materials by hindering the propagation of dislocation. Orowan dispersed barrier model has been widely applied to estimate the strength increment from radiation-induced defects. The model illustrated the interaction between glide dislocations and a variety of obstacles, including precipitates, voids, and dislocation loops. In this study, the change of yield stress $\Delta\sigma_y$ is contributed from voids $\Delta\sigma_v$ and dislocation loops $\Delta\sigma_l$, which is:

$$\Delta\sigma_y = \Delta\sigma_v + \Delta\sigma_l \tag{4.3}$$

Orowan hardening model for polycrystalline material stated that the increment of strength could be obtained by the size and number density of a specific obstacle:

$$\Delta\sigma_j = \alpha M \mu b \sqrt{N_j d_j} \tag{4.4}$$

$$\mu = \frac{E}{2(1+\nu)} \tag{4.5}$$

where α is a constant represents the strength of the specific barrier, $\alpha = 0.5$ for both void and dislocation loop. The value of α for loops was derived by strengthening data in reference [53]. Ando et al. [54] found void shearing is more likely than Orowan pinning, which is the same as the observation in irrAM-316L compressed pillar TEM micrograph in Figure 50b. The void shearing leads to a value of $\alpha = 0.5$ rather than 1.0. M is the Taylor factor to represent the average behavior of polycrystalline material. Since single crystal pillars were analyzed in this study, Schmid factor m will be used instead. μ is the shear modulus of the material, 80 GPa for 316L SS. b is Burgers vector of the interacting dislocation. N is the number density of obstacle. d is the size of the obstacle. Subscript j represents obstacle type, v for void or l for dislocation loop. Since all the pillars are single crystal with known Schmid factor. The Orowan equation can be expressed by the change of critical shear stress shown in equation (4.6).

$$\Delta\tau_j = \alpha_j \mu b \sqrt{N_j d_j} \tag{4.6}$$

Void and dislocation loop size and density were obtained from the TEM results. The dislocation density used in radiation hardening calculation should be four times higher than the number from TEM measurement since the imaging condition can only acquire one variant of dislocation loops. The calculated τ_{crss} of irradiated variant is the sum of

$\tau_{vir316L} + \Delta\tau_{crss}$, which is about 244 MPa. The calculated result agreed well with the experiment measurement, which is 246 MPa.

With the same method, the τ_{crss} for 0.35 dpa irradiated sample can be obtained, which is 231 MPa. The results are summarized in Table 6, showing the dislocation loop was the primary factor in strengthening the AM 316L SS. The calculated τ_{crss} for the 0.35 dpa sample does not significantly differ from the 1.80 dpa sample. From the TEM analysis results in Table 3, void size increased while number density decreased. The decrease of void number density reduced the contribution to irradiation hardening. For dislocation loops contribution, number density increased by about 22% while the size remained unchanged, showing the sign of dislocation loop saturation. The saturation lowers the difference of irradiation hardening between 1.80 dpa and 0.35 dpa samples.

Table 6 Irradiation hardening from voids, dislocation loops, and the sum increment for irrAM-316L 1.80 dpa and 0.35 dpa samples.

	1.80 dpa	**0.35 dpa**
$\Delta\tau_{crss-v}$ **(MPa)**	38	36
$\Delta\tau_{crss-l}$ **(MPa)**	119	108
$\Delta\tau_{crss-v} + \Delta\tau_{crss-l}$ **(MPa)**	157	144
$\tau_{vir316L} + \Delta\tau_{crss}$ **(MPa)**	244	231
Experiment CRSS (MPa)	246	--

4.5 Conclusion

The study showed that microstructural details such as pores introduced during the manufacturing played a crucial role in determining yield strength, as observed by dislocation bowing in TEM characterization. The residual stress after the manufacturing leads to a noticeable hardening. The hardening effects can be removed by applying thermal annealing. Proton irradiation increases the resolved critical stress on dislocation gliding on (111) plane. Both voids and dislocations contributed to the hardening. Due to size difference, irradiation-induced voids behave differently from large pores from the manufacturing. Void deformation, elongation, and cutting by dislocations were observed in the ion-irradiated sample. Irradiation hardening facilitated twinning, while large manufacturing-induced pore blocked twinning propagation. The hardening can be well explained by defect strengthening mechanism, based on density and size of voids and dislocations measured using TEM.

CHAPTER V

SUMMARY AND PERSPECTIVE OF FUTURE DEVELOPMENT OF ADDITIVE MANUFACTURING

The flexibility of additive manufacturing possesses an excellent potential for this technology. Not merely repairing existing parts, AM technologies can build new types of materials with innovative properties. However, the manipulation of the microstructure is not fully understood. Operating parameters can significantly change the microstructure and mechanical properties. The difficulty in controlling the cooling rate also makes the uniform microstructure hard to achieve as the cooling rate varies as the geometry and volume of the product change. AM process introduces the features not found in traditional materials, including pores and sub-grain boundaries. Pores can be created by the gap between layers or scan path. Sub-grain boundaries are the results of residual stress brought by a high cooling rate. Oliveira et al. created a simplified diagram to show the parameters to fabricate fully dense materials [55]. In this study, although the pores were found hindering the propagation of dislocation, residual stress dominates the mechanical properties of as-manufactured AM-316L. This observation was based on the AM-316L CRSS change after post heat treatment. The CRSS decreased to the wrought 316L SS region after annealing, which is between 80 MPa to 90 MPa [46], indicating the residual stress in AM-316L had a more significant impact on mechanical properties. The low number density might make the strengthening from pores negligible. The response of AM-316L under irradiation may be applied to the same concept. The residual stress and sub-grain boundary should be the dominant factors in AM-316L radiation tolerance. Saboori et al. briefly summarized the relationship of sub-grain structure and printing factors [56]. The size and morphology of the sub-grain structure vary with the parameters. Since the evolution of sub-grain boundaries is highly tied with the mechanical properties, this could bring compatibility and uniformity issues while fabricating functionally graded materials. It is expected that the studies on how printing parameters influence the sub-grain structures will pose a great impact on AM technologies' development.

REFERENCES

1. Mansur, L.K., *Theory and experimental background on dimensional changes in irradiated alloys.* Journal of Nuclear Materials, 1994. **216**: p. 97-123.
2. Whittle, K., *Nuclear fuel, part 2: operational effects.* 2053-2563, 2016: p. 4-1 to 4-18.
3. Joel, C.N., R. Sajjad, and T. Andres, *2 - Review of additive manufacturing technologies and applications in the aerospace industry.* 2019: p. 7-31.
4. Was, G., *Fundamentals Of Radiation Materials*. 2007: Springer.
5. Toby, B.H. and R.B. Von Dreele, *GSAS-II: the genesis of a modern open-source all purpose crystallography software package.* Journal of Applied Crystallography, 2013. **46**(2): p. 544-549.
6. Stutzman, P.E. and L. Struble, *Instructions in Using GSAS Rietveld Software for Quantitative X-ray Diffraction Analysis of Portland Clinker and Cement*, in *Technical Note 1884*. 2015, National Institute of Standards and Technology.
7. Luo, Z., et al., *Pawley and Rietveld refinements using electron diffraction from L1(2)-type intermetallic Au(3)Fe(1)-x nanocrystals during their in-situ order-disorder transition.* Ultramicroscopy, 2011. **111**(8): p. 1295-304.
8. L. B. McCusker, R.B.V.D., D. E. Cox, D. LoueÈrd and P. Scardie, *Rietveld refnement guidelines.* Journal of Applied Crystallography, 1999. **32**: p. 36-50.
9. P. THOMPSON, D.E.C.A.J.B.H., *Rietveld refinement of Debye-Scherrer synchrotron X-ray data from Al2O3.* Journal of Applied Crystallography, 1987. **20**: p. 79-83.

10. Toby, B.H., *R factors in Rietveld analysis: How good is good enough?* Powder Diffraction, 2012. **21**(1): p. 67-70.

11. Wisniewski, W. and C. Russel, *An experimental viewpoint on the information depth of EBSD.* Scanning, 2016. **38**(2): p. 164-71.

12. Edwards, D.J., et al., *Influence of irradiation temperature and dose gradients on the microstructural evolution in neutron-irradiated 316SS.* Journal of Nuclear Materials, 2003. **317**(1): p. 32-45.

13. Jenkins, M.L., *Characterisation of radiation-damage microstructures by TEM.* Journal of Nuclear Materials, 1994. **216**: p. 124-156.

14. Mitchell, D.R.G., *Determination of mean free path for energy loss and surface oxide film thickness using convergent beam electron diffraction and thickness mapping a case study using Si and P91 steel.* Journal of Microscopy, 2006. **224**: p. 187-196.

15. T. Malis, S.C.C., and R.F. Egerton, *EELS Log-Ratio Technique for Specimen-Thickness Measurement in the TEM.* Journal of Electron Microscopy Technique, 1988. **8**: p. 193-200.

16. Iakoubovskii, K., et al., *Thickness measurements with electron energy loss spectroscopy.* Microscopy Research and Technique, 2008. **71**(8): p. 626-631.

17. Cooper, D., et al., *Strain measurement for the semiconductor industry with nm-scale resolution by dark field electron holography and nanobeam electron diffraction.* Journal of Physics: Conference Series, 2011. **326**.

18. Darbal, A.D., et al., *Applications of Automated High Resolution Strain Mapping in TEM on the Study of Strain Distribution in MOSFETs.* Microscopy and Microanalysis, 2014. **20**(S3): p. 1066-1067.

19. Tanaka, M. *Precession electron diffraction.* Available from: https://www.jeol.co.jp/en/words/emterms/search_result.html?keyword=precession%20electron%20diffraction.

20. Zhang, X., et al., *Evolution of Microstructure, Residual Stress, and Tensile Properties of Additively Manufactured Stainless Steel Under Heat Treatments.* JOM, 2020.

21. G. S. Was, R.S.A., *Radiation damage using ion beams*, in *Comprehensive Nuclear Materials*. 2012, Elsevier Ltd. p. 195--221.

22. *ASTM Standard E521-16, " Standard Practice for Investigating the Effects of Neutron Radiation Damage Using Charged-Particle Irradiation".* ASTM International, West Conshohocken, PA, 2016.

23. Saboori, A., et al., *An investigation on the effect of powder recycling on the microstructure and mechanical properties of AISI 316L produced by Directed Energy Deposition.* Materials Science and Engineering: A, 2019. **766**.

24. Song, M., et al., *Radiation damage and irradiation-assisted stress corrosion cracking of additively manufactured 316L stainless steels.* Journal of Nuclear Materials, 2019. **513**: p. 33-44.

25. Gan, J., et al., *The effect of oversized solute additions on the microstructure of 316SS irradiated with 5 MeV Ni++ ions or 3.2 MeV protons.* Journal of Nuclear Materials, 2004. **325**(2-3): p. 94-106.

26. Sencer, B.H., et al., *Proton irradiation emulation of PWR neutron damage microstructures in solution annealed 304 and cold-worked 316 stainless steels.* Journal of Nuclear Materials, 2003. **323**(1): p. 18-28.

27. Xu, C., et al., *Microstructural evolution of NF709 austenitic stainless steel under in-situ ion irradiations at room temperature, 300, 400, 500 and 600 °C.* Journal of Nuclear Materials, 2018. **509**: p. 644-653.

28. Liu, X., et al., *A transmission electron microscopy study of EBR-II neutron-irradiated austenitic stainless steel 304 and nickel-base alloy X-750.* Journal of Nuclear Materials, 2020. **528**: p. 151851.

29. Barr, C.M., et al., *Anisotropic radiation-induced segregation in 316L austenitic stainless steel with grain boundary character.* Acta Materialia, 2014. **67**: p. 145-155.

30. Okamoto, P.R. and H. WIEDERSICH, *Segregation of alloying elements to free surfaces during irradiation.* JOURNAL OF NUCLEAR MATERIALS, 1974. **53**: p. 336-345.

31. Tamura, I., *Deformation-induced martensitic transformation and transformation-induced plasticity in steels.* Metal Science, 1982. **16**(5): p. 245-253.

32. Manikandan, S.G.K., D. Sivakumar, and M. Kamaraj, *Welding the Inconel 718 Superalloy*, ed. C. Gifford. 2019: Elsevier. 53-186.

33. Javanbakht, M., et al., *The effect of a pre-existing nanovoid on martensite formation and interface propagation: a phase field study.* Mathematics and Mechanics of Solids, 2020.

34. Pham, M.S., B. Dovgyy, and P.A. Hooper, *Twinning induced plasticity in austenitic stainless steel 316L made by additive manufacturing.* Materials Science and Engineering: A, 2017. **704**: p. 102-111.

35. Wang, Y.M., et al., *Additively manufactured hierarchical stainless steels with high strength and ductility.* Nature Materials, 2018. **17**(1): p. 63-71.

36. Han, W.Z., et al., *Helium Nanobubbles Enhance Superelasticity and Retard Shear Localization in Small-Volume Shape Memory Alloy.* Nano Lett, 2017. **17**(6): p. 3725-3730.

37. Gussev, M.N., D.A. McClintock, and F.A. Garner, *Analysis of structure and deformation behavior of AISI 316L tensile specimens from the second operational target module at the Spallation Neutron Source.* Journal of Nuclear Materials, 2016. **468**: p. 210-220.

38. Hojná, A., *Overview of Intergranular Fracture of Neutron Irradiated Austenitic Stainless Steels.* Metals, 2017. **7**(10): p. 392.

39. Mao, K.S., et al., *Role of cavities on deformation-induced martensitic transformation pathways in a laser-welded, neutron irradiated austenitic stainless steel.* Scripta Materialia, 2020. **178**: p. 1-6.

40. K.K. Kadyrzhanov, O.P.M., *Martensitic Transformations in Neutron Irradiated and Helium Implanted Stainless*. Journal of ASTM International, 2004. **April 2004 Vol. 1**(No. 4).

41. Shang, Z., et al., *Response of solidification cellular structures in additively manufactured 316 stainless steel to heavy ion irradiation: an in situ study*. Materials Research Letters, 2019. **7**(7): p. 290-297.

42. Bringa, E.M., et al., *Are nanoporous materials radiation resistant?* Nano Lett, 2012. **12**(7): p. 3351-5.

43. Sun, C., et al., *In situ study of defect migration kinetics in nanoporous Ag with enhanced radiation tolerance*. Sci Rep, 2014. **4**: p. 3737.

44. Chen, Y., et al., *Damage-tolerant nanotwinned metals with nanovoids under radiation environments*. Nature Communications, 2015. **6**: p. 7036.

45. McMurtrey, M., et al., *Investigation of the irradiation effects in additively manufactured 316L steel resulting in decreased irradiation assisted stress corrosion cracking susceptibility*. Journal of Nuclear Materials, 2021. **545**.

46. Monnet, G. and M.A. Pouchon, *Determination of the critical resolved shear stress and the friction stress in austenitic stainless steels by compression of pillars extracted from single grains*. Materials Letters, 2013. **98**: p. 128-130.

47. Shen, Y.F., et al., *Twinning and martensite in a 304 austenitic stainless steel*. Materials Science and Engineering: A, 2012. **552**: p. 514-522.

48. Gussev, M.N. and K.J. Leonard, *In situ SEM-EBSD analysis of plastic deformation mechanisms in neutron-irradiated austenitic steel.* Journal of Nuclear Materials, 2019. **517**: p. 45-56.

49. Byun, T.S., et al., *Strain hardening and plastic instability properties of austenitic stainless steels after proton and neutron irradiation.* Journal of Nuclear Materials, 2001. **298**(3): p. 269-279.

50. LEE, E.H., et al., *On the origin of deformation microstructures in austenitic stainless steel: part I—microstructures.* Acta Materialia, 2001. **49**(16): p. 3269-3276.

51. LEE, E.H., et al., *On the origin of deformation microstructures in austenitic stainless steel: Part II—Mechanisms.* Acta Materialia, 2001. **49**(16): p. 3277-3287.

52. Byun, T.S., *On the stress dependence of partial dislocation separation and deformation microstructure in austenitic stainless steels.* Acta Materialia, 2003. **51**(11): p. 3063-3071.

53. Hashimoto, N., E. Wakai, and J.P. Robertson, *Relationship between hardening and damage structure in austenitic stainless steel 316LN irradiated at low temperature in the HFIR.* Journal of Nuclear Materials, 1999. **273**(1): p. 95-101.

54. Ando, M., et al., *The contribution of various defects to irradiation-induced hardening in an austenitic model alloy.* Journal of Nuclear Materials, 2000. **283-287**: p. 423-427.

55. Oliveira, J.P., A.D. LaLonde, and J. Ma, *Processing parameters in laser powder bed fusion metal additive manufacturing.* Materials & Design, 2020. **193**.

56. Saboori, A., et al., *Microstructure and Mechanical Properties of AISI 316L Produced by Directed Energy Deposition-Based Additive Manufacturing: A Review*. Applied Sciences, 2020. **10**(9).